

High-frequency asymptotics of the vertex function: diagrammatic parametrization and algorithmic implementation

Nils Wentzell,^{1,2} Gang Li,¹ Agnese Tagliavini,^{1,2} Ciro Taranto,³ Georg Rohringer,^{1,4,5} Karsten Held,¹ Alessandro Toschi,¹ and Sabine Andergassen²

¹*Institute for Solid State Physics, Vienna University of Technology, 1040 Vienna, Austria*

²*Institut für Theoretische Physik and Center for Quantum Science,
Universität Tübingen, Auf der Morgenstelle 14, 72076 Tübingen, Germany*

³*Max-Planck-Institute for Solid State Research, 70569 Stuttgart, Germany*

⁴*Russian Quantum Center, 143025 Skolkovo, Russia*

⁵*Department of Physics, M.V. Lomonosov Moscow State University, 119991 Moscow, Russia*

Vertex functions are a crucial ingredient of several forefront many-body algorithms in condensed matter physics. However, the full treatment of their frequency and momentum dependence severely restricts numerical calculations. A significant advancement requires an efficient treatment of the high-frequency asymptotic behavior of the vertex functions. In this work, we first provide a detailed diagrammatic analysis of the high-frequency structures and their physical interpretation. Based on these insights, we propose a parametrization scheme, which captures the whole high-frequency domain for arbitrary values of the local Coulomb interaction and electronic density, and we discuss the details of its algorithmic implementation in many-body solvers based on parquet-equations as well as functional renormalization group schemes. Finally, we assess its validity by comparing our results for a single impurity Anderson model with exact diagonalization calculations. The proposed parametrization is pivotal for the algorithmic development of all quantum many-body methods based on vertex functions arising from local microscopic interactions, such as the diagrammatic approaches including spatial correlations beyond dynamical mean-field theory.

PACS numbers: 71.10.Fd, 71.10-w, 71.27.+a

I. INTRODUCTION

One of the most challenging aspects in contemporary condensed matter research is the theoretical treatment of correlation effects in the non-perturbative regime. While the state-of-the-art theoretical tools allow for an accurate treatment of quantum many-body correlations in specific cases, their reliability is not guaranteed in general and is often limited to particular parameter regimes. In the last decade, several promising quantum field theoretical schemes have been proposed, but their actual implementation calls for a significant improvement of the current algorithmic procedures. In particular, most of the novel non-perturbative schemes are based on a Feynman diagrammatic expansion around a correlated starting point. This means to replace the bare electronic interaction with a dynamical effective one and the bare propagators by dressed ones, which includes non-perturbatively, through the two-particle vertex function and the self-energy, a significant part of the correlations from the very beginning. The numerical treatment of these vertex functions is, however, numerically very demanding, and the development of efficient ways to include them in the current algorithms is mandatory.

The two-particle vertex, recently object of several focused studies,^{1–8} depends in general on three independent frequencies and momenta, and additionally on spin and orbital variables. Even in the $SU(2)$ symmetric case, the efficient computation of two-particle vertices becomes very challenging for a reasonably large system at low temperatures. Besides the storage, the inclusion of the

asymptotic structure during the computation represents a major issue and requires to exploit a detailed understanding of its underlying structure^{4–7} in order to reduce the numerical effort⁸.

To this aim, we begin by presenting a detailed diagrammatic analysis of the frequency and momentum structures of the vertex functions, focusing on the algorithmic aspects relevant for the development of improved parametrization schemes. After defining the general guidelines of the algorithmic implementation, we present applications for many-body solvers based on functional renormalization group⁹ (fRG) schemes as well as parquet equations^{1,8,10,11}. In particular, the validity of the proposed parametrization algorithm could be quantitatively assessed by comparing our results for the single impurity Anderson model (SIAM) obtained by means of fRG and the parquet approximation¹² (PA) with exact diagonalization (ED) calculations. We emphasize that the identification of the relevant asymptotic structures of the vertex functions in frequency and momentum space and the resulting reduced parametrizations are extremely valuable for an efficient implementation of several other many-body approaches beyond fRG & PA, such as the dynamical vertex approximation^{13–17,8} (DFA), the one-particle irreducible approach¹⁸, DMF²RG,¹⁹ dual fermion^{20–25} (DF), TRILEX^{26,27} and QUADRILEX²⁸.

The paper is organized as follows: We introduce the formalism and notation at the two-particle level in Sec. II, and the parametrization of the asymptotics in Sec. III. The generic implementation is presented in Sec. IV, with some technical details specified in the appendices. After

a short discussion of analytical results obtained in the atomic limit, we describe the specific implementations for the fRG and the parquet solvers. In Sec. V we then provide a discussion of the obtained results together with a comparison to exact results of the SIAM. A conclusion and outlook is eventually provided in Sec. VI.

II. DIAGRAMMATIC FORMALISM AT THE TWO-PARTICLE LEVEL

In this section we present a concise summary of the general formalism for two-particle vertex functions and of their generic frequency and momentum structures. In particular, we recall how their high-frequency asymptotic behavior can be qualitatively related to the lowest-order perturbation theory diagrams. While a comprehensive investigation of the physical interpretation of the different structures can be found in Sec. III and in Refs. [4,7], we focus here mainly on aspects which are relevant for the algorithmic development and the applications presented in this paper.

Although most of the following considerations are valid for a wide range of many-body Hamiltonians, we will restrict ourselves, for the sake of notational simplicity, to one-band systems with a local Coulomb interaction. Specifically, we consider the following Hamiltonian:

$$\hat{\mathcal{H}} = \sum_{ij,\sigma} t_{ij} (\hat{c}_{i\sigma}^\dagger \hat{c}_{j\sigma} + \hat{c}_{j\sigma}^\dagger \hat{c}_{i\sigma}) + \sum_i U_i \hat{n}_{i\uparrow} \hat{n}_{i\downarrow}, \quad (1)$$

where $\hat{c}_{i\sigma}^{(\dagger)}$ annihilates (creates) an electron with spin σ at the lattice site \mathbf{R}_i and $\hat{n}_{i\sigma} = \hat{c}_{i\sigma}^\dagger \hat{c}_{i\sigma}$. The hopping amplitude for an electron between the lattice sites i and j is denoted by t_{ij} (for $i = j$ this corresponds to setting the energy-level for an electron at site i), while U_i is a (site-dependent) local interaction between electrons of opposite spin.

From the Hamiltonian in Eq. (1) one retains the standard Hubbard model by choosing the parameters $t_{ij} = -t$ if i and j are nearest neighbors and $t_{ij} = 0$ otherwise, and $U_i = U$ (site independent). The restriction $t_{ij} = V_j \delta_{i0}$, $t_{ii} = \varepsilon_i/2$ and $U_i = U \delta_{i0}$, on the other hand, corresponds to the SIAM, where lattice site \mathbf{R}_0 is the impurity.

In the following we will consider the two-particle Green's function for the model in Eq. (1), where for the SIAM we will restrict ourselves to the corresponding (purely local) correlation functions at the impurity site. Considering the time- and for the Hubbard model also space- translational invariance of the system, we can work more conveniently in frequency (and momentum) space. To this end, we will adopt both for the SIAM and the Hubbard model the following generalized notation for the frequency and momentum arguments of the Green's functions: k denotes a generalized fermionic, q a generalized bosonic index. For the Hubbard model, this corresponds to the four-vector notation $k = (\nu, \mathbf{k})$ and

$q = (\Omega, \mathbf{q})$, where ν is a fermionic and Ω a bosonic Matsubara frequency and \mathbf{k} and \mathbf{q} are momenta in the first Brillouin zone. In the case of the SIAM, k and q correspond simply to the fermionic and bosonic Matsubara frequencies ν and Ω , respectively.

The general definition of the two-particle Green's function G_2 is given explicitly in Appendix A, together with the general relation between the two-particle Green's function and the (full) vertex function F . The latter is obtained from G_2 by first removing all unconnected parts, and by subsequently amputating all outer legs²⁹. From a physical perspective, F represents the quasi-particle scattering rate between particles and holes (in parameter regimes where such excitations are well-defined²⁹). Diagrammatically, F consists of all connected two-particle diagrams, i.e., all (connected) Feynman diagrams with *two incoming* and *two outgoing* lines (see leftmost diagram in Fig. 1).

One can now decompose the full vertex F into *four* distinct classes of diagrams, that differ in their two-particle irreducibility^{1,10,11}. Specifically, a vertex diagram is coined *fully two-particle irreducible* if it cannot be split into two parts by cutting any two internal lines. An example for such a diagram is the second diagram in the upper line of Fig. 1. The sum of all diagrams exhibiting this property is denoted as Λ_{2PI} . On the other hand, if a vertex diagram can be separated by cutting two lines, it is referred to as *two-particle reducible*. However, this notion of reducibility is obviously more complicated than in the one-particle situation. In fact, there are *three* possible scenarios for the separation of a diagram. The third, fourth and fifth diagram in the first row of Fig. 1 illustrate this state of affairs: (i) In the third diagram the two incoming particles can be separated from the two outgoing ones by cutting the two Green's functions and, hence, this diagram is coined *particle-particle* reducible. The diagrams of this type sum up to the reducible vertex function Φ_{pp} . (ii) In the fourth diagram of Fig. 1, the lower incoming particle and hole can be separated from the corresponding upper ones. The sum of all such longitudinal particle-hole reducible diagrams is referred to as Φ_{ph} . (iii) Finally, the rightmost diagram can be split in such a way, that one part contains the lower incoming particle and the upper incoming hole and vice versa for the second part. Such diagrams are reducible in the transverse particle-hole channel, and belong to the subset $\Phi_{\overline{ph}}$ of the full vertex F .

It is important to stress that each diagram for the full vertex F belongs to *exactly one* of the four classes: Either it is fully two-particle irreducible (Λ_{2PI}) or it is reducible in the *pp*-channel (Φ_{pp}), in the longitudinal *ph*-channel (Φ_{ph}) or in the transverse *ph*-channel¹ ($\Phi_{\overline{ph}}$). Conse-

¹ The orientation of *ph* and \overline{ph} diagrams (horizontal/vertical) is directly linked to the arrangement of the external indices, and is thus a matter of convention.

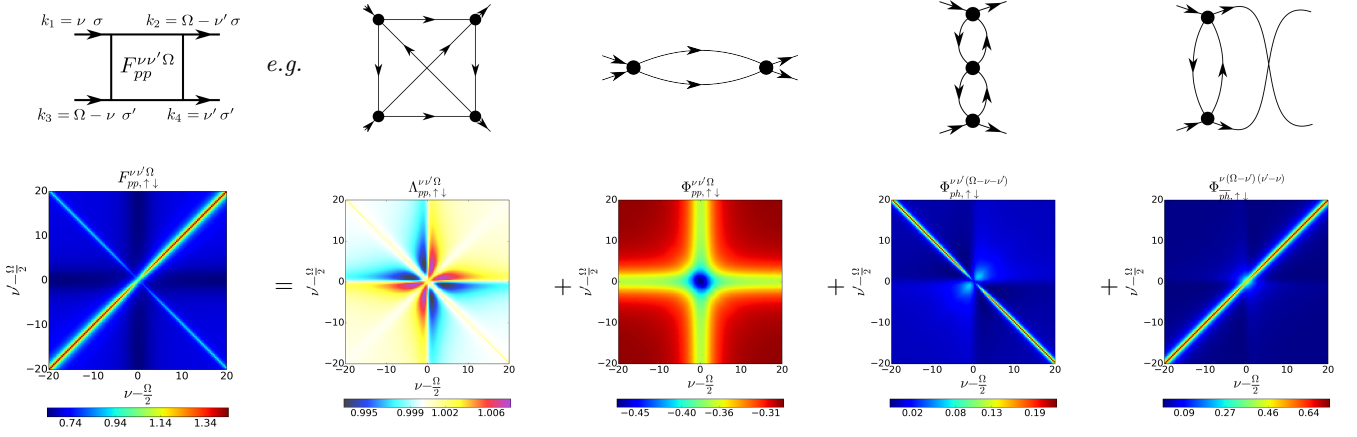


FIG. 1: The upper row shows full vertex $F_{\uparrow\downarrow}$ in pp -notation, and the lowest order diagrams (excluding the bare interaction) included in the contributions from the different vertex functions. The bottom row shows the numerical SIAM results for these vertices ($U = 1$, $\beta = 20$, $\Delta(0) = D = 1$) and their connection through the parquet equation (2) using pp -notation for vanishing transfer frequency $\Omega = 0$. Notations according to Appendix A. In the diagrammatic representations used throughout this paper, all external legs are to be considered as the remainder of the amputated propagators.

quently, by summing up all four contributions one retrieves the full two-particle scattering amplitude F :

$$F = \Lambda_{2\text{PI}} + \Phi_{pp} + \Phi_{ph} + \Phi_{\overline{ph}}. \quad (2)$$

which is known as *parquet equation*^{1,10,11}. It represents a *single* relation for the five quantities F , $\Lambda_{2\text{PI}}$ and Φ_r , with $r \in \{pp, ph, \overline{ph}\}$. Hence, supposed that one of them is known, e.g., the full vertex F , three more relations are necessary to calculate all remaining vertices. To this end we note that we can group together all diagrams which are *not* reducible, i.e., irreducible, in a given channel r , and denote them as Γ_r :

$$\Gamma_r = \Lambda_{2\text{PI}} + \sum_{r' \neq r} \Phi_{r'}, \quad (3)$$

According to Eq. (2) it is then obvious that

$$F = \Gamma_r + \Phi_r, \quad (4)$$

for all three channels r . Eqs. (4) are referred to as Bethe-Salpeter (BS) equations. The crucial observation is now that Φ_r can be expressed by means of a ladder construction in the given channel r in terms of F and Γ_r as it is depicted in Fig. 2. Schematically written, this means that $\Phi_r \sim \Gamma_r GGF$, where G denotes a single-particle Green's function (see also Appendix B). This relation closes the set of Eqs. (2) and (4). Let us note that the explicit frequency/momentum and spin dependent form of the BS equations is rather involved^{4,8,18} and we refer the reader to Appendix B for its specific definitions in all three scattering channels.

Let us remark that for the most efficient treatment of the BS equations, the natural frequency (and momentum) convention in their respective channel r should be adopted. This means that the energy and momentum

which is transferred via the ladder (see Fig. 2) is given by the bosonic index q . In the particle-particle notation this is exactly the case for the choice depicted in the first diagram of Fig. 1: Here, the two particles with the frequencies (momenta) k and $q - k$ scatter and transfer the energy (momentum) q to the system. Hence, we refer to the frequency convention indicated in this figure as particle-particle (pp) notation. The corresponding natural frequency convention for the longitudinal particle-hole channel (ph) can be obtained from the latter one simply by replacing $q \rightarrow q + k + k'$. Finally, for the transverse particle-hole channel (\overline{ph}) the natural frequency/momentum convention is derived from the pp -one by the shifts $k' \rightarrow k + q$ and $q \rightarrow k + k' + q$.

In their natural frequency/momentum convention the BS equations can be written as simple matrix multiplications in the frequency/momentum space^{1,4}. Hence, in the following, we will assume that the corresponding irreducible and reducible vertex functions Γ_r and Φ_r in the three channels $r \in \{pp, ph, \overline{ph}\}$ always depend on their natural frequency/momentum arguments. However, for the parquet equation (2), all vertex functions must be considered in the *same* representation which, hence, re-

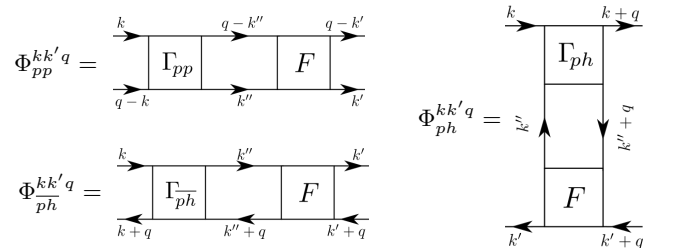


FIG. 2: Compact diagrammatic representation of the Bethe-Salpeter equations in all scattering channels. Each k'' is integrated over.

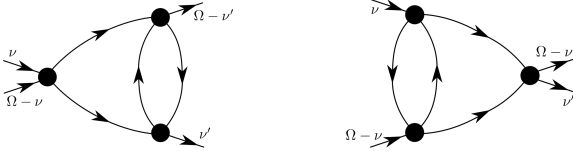


FIG. 3: The so called “eye”-diagrams in the pp channel.

quires the inverse of the aforementioned shifts in their frequency/momentum arguments. This corresponds exactly to the choice of frequency arguments in the vertex functions of Fig. 1.

In the lower panels of Fig. 1 the dependence of the local vertex functions $F_{\uparrow\downarrow}$, $\Lambda_{2\text{PI},\uparrow\downarrow}$ and $\Phi_{r,\uparrow\downarrow}$ on the fermionic frequency arguments ν and ν' is shown, where the pp -notation for vanishing transfer frequency $\Omega = 0$ is used. While we restrict ourselves here to the $\uparrow\downarrow$ spin combination, we stress that analogous features are found also in $F_{pp,\uparrow\uparrow}^{\nu\nu'(\Omega=0)}$ and even at finite transfer frequencies $\Omega \neq 0$. Investigating the full vertex $F_{pp,\uparrow\downarrow}^{\nu\nu'(\Omega=0)}$ (leftmost panel) we can identify three main features: (i) There is a constant background *different* from the (constant) bare Coulomb interaction U . (ii) We observe two diagonal structures which we will refer to as main (for $\nu = \nu'$) and secondary (for $\nu = -\nu'$) diagonal. (iii) $F_{pp,\uparrow\downarrow}^{\nu\nu'(\Omega=0)}$ exhibits also a “plus”-like structure, i.e., an enhanced scattering rate along the lines $\nu = \pm\pi/\beta$ and $\nu' = \pm\pi/\beta$. Remarkably, these features do *not* decay, even in the limit of large fermionic frequencies and give, hence, rise to a highly non-trivial asymptotic behavior of the vertex functions. In order to explain their origin, we will analyze in the following the frequency structures of the four building blocks of F , i.e., of the fully irreducible vertex $\Lambda_{2\text{PI}}$ and its corresponding reducible counterparts Φ_r . Our strategy will be guided by the comprehension of the frequency behavior of the lowest order perturbation diagrams for each of these sub-parts of the full vertex.

As for the fully irreducible vertex $\Lambda_{2\text{PI},pp,\uparrow\downarrow}^{\nu\nu'(\Omega=0)}$, we can see that it decays uniformly in all directions of the two-dimensional (Matsubara) frequency space. Hence, $\Lambda_{2\text{PI},pp,\uparrow\downarrow}^{\nu\nu'(\Omega=0)}$ does not contribute to the asymptotic structures of the two-particle scattering amplitude $F_{pp,\uparrow\downarrow}^{\nu\nu'(\Omega=0)}$ (except for the trivial constant background given by the interaction U). Beyond this numerical observation, the asymptotic behavior of $\Lambda_{2\text{PI}}$ can be justified also through the analysis of its diagrammatic structure, exemplified by the “envelope”-diagram (second diagram from the left in Fig. 1). As it has been discussed in detail in Ref. [4], $\Lambda_{2\text{PI},pp}$ does indeed depend explicitly on ν and ν' (and Ω) and, hence, it decays for a large value for any of its frequency arguments².

Turning to the diagrams reducible in the particle-particle scattering channel, i.e., $\Phi_{pp,\uparrow\downarrow}^{\nu\nu'(\Omega=0)}$ (third panel in Fig. 1), they exhibit *two* of the three asymptotic frequency structures of $F_{pp,\uparrow\downarrow}^{\nu\nu'(\Omega=0)}$. Specifically, one can identify a constant background and a well-defined “plus”-structure. The background can be immediately understood by analyzing the second order diagram depicted above the plot of $\Phi_{pp,\uparrow\downarrow}$. This is given by the bubble-term

$$\frac{U^2}{\beta} \sum_{\nu_1} G(\nu_1) G(\Omega - \nu_1), \quad (5)$$

which -evidently- does not depend explicitly on ν and ν' . Hence, bubble diagrams of this type are responsible for the constant background observed in the particle-particle reducible vertex, and, consequently, in the full vertex F . The “plus”-structure, on the other hand, originates, in lowest order, from the so-called “eye”-diagrams (see Fig. 3), which either on their left or on their right hand side collapse into a bare vertex U . For this reason (as detailed in Sec. III), they cannot explicitly depend on both ν and ν' , thus remaining constant upon increasing the corresponding (unnecessary) frequency⁴.

Let us now consider the vertex function reducible in the particle-hole (longitudinal) channel, i.e., $\Phi_{ph,\uparrow\downarrow}^{\nu\nu'(\Omega-\nu-\nu')}$ (fourth density plot from the left in Fig. 1). One can clearly see that this vertex exhibits a secondary diagonal structure along $\nu' = -\nu$. Again, we can gain insight about the origin of this feature by analyzing the lowest order in U perturbative diagram of this vertex. For the $\uparrow\downarrow$ -channel considered here, this is of third order in U , as the bare bubble term vanishes as a result of spin conservation. It is given by the fourth diagram (from the left) in Fig. 1, and reads (pp -notation)

$$\frac{U^3}{\beta^2} \left[\sum_{\nu_1} G(\nu_1) G(\nu_1 - \Omega + \nu + \nu') \right]^2, \quad (6)$$

i.e., it depends only on the ph transfer frequency $\Omega - \nu - \nu'$ rather than the two fermionic frequencies ν and ν' separately. Consequently, for fixed pp transfer Ω , its value remains constant along a line $\Omega - \nu - \nu' = \text{const}$ and, thus, generates the secondary diagonal structure.

Finally, we turn our attention to the vertex reducible in the transverse particle-hole channel, $\Phi_{ph,\uparrow\downarrow}^{\nu(\Omega-\nu')(\nu'-\nu)}$. Obviously, it accounts for the main diagonal in the full scattering amplitude $F_{pp,\uparrow\downarrow}^{\nu\nu'(\Omega=0)}$. Once again, the analysis of its lowest order (bubble) contribution allows for an intuitive explanation of this feature. It is given by the last

² Every frequency dependence of a diagram originates from the

frequency dependence of the corresponding Green's functions. The latter decay in the asymptotic high frequency regime as $1/i\nu$.

diagram in Fig. 1, which reads explicitly (pp -notation)

$$\frac{U^2}{\beta} \sum_{\nu_1} G(\nu_1) G(\nu_1 + \nu' - \nu), \quad (7)$$

and depends only on the \overline{ph} transfer frequency $\nu' - \nu$. Consequently, its value remains constant along a line $\nu' - \nu = \text{const}$ and, hence, generates the main diagonal structure.

The above analysis demonstrates that the high-frequency asymptotic features of the vertex functions in the weak coupling regime are determined at the second and third order in U by two-particle reducible bubble- and “eye”-like diagrams. A generalization of these conclusions to the non-perturbative regime will be discussed in the following Section.

III. PARAMETRIZATION OF THE ASYMPTOTICS

In the following, we will generalize the discussion of the previous section about the main (asymptotic) structures of the various vertex functions to the non-perturbative situation. To this end, we first note that the reduced complexity of specific diagrams regarding their frequency and momentum dependence is *not* a peculiarity of low(est) order perturbation theory but rather a general consequence of the frequency and momentum independence of the bare Coulomb (Hubbard) interaction U . In fact, if any two external lines of the vertex, e.g., the incoming momenta and frequencies k_1 and k_3 , are attached to the same bare vertex U , energy and momentum conservation requires $k_1 + k_3 = k' + k''$ where k' and k'' denote internal frequencies/momenta which are summed. Obviously, in this situation the entire diagram does depend only on the linear combination $k_1 + k_3$ rather than k_1 and k_3 separately. Such a behavior has been already observed for lowest order perturbative (bubble and “eye”) diagrams in the previous section, and does not change, as a matter of course, upon dressing these diagrams by means of vertex corrections. These insights hence suggest the following subdivision of the reducible vertex function $\Phi_{pp}^{kk'q}$ (and correspondingly for the other two channels) into three distinct classes, that are depicted diagrammatically in Fig. 4:

- Class 1: The ingoing *and* outgoing frequencies/momenta are attached to the same bare vertex. These diagrams correspond to (dressed) bubble diagrams (see first line of Fig. 4), and can hence be parametrized by a *single* (bosonic) transfer frequency and momentum $q = k_1 + k_3$. The sum of all diagrams of this class will be denoted by $\mathcal{K}_{1,pp}^q$.
- Class 2: Either the incoming *or* the outgoing frequencies/momenta are attached to the same bare vertex. These diagrams correspond to (dressed) eye diagrams (see, e.g., Fig. 3 and first two diagrams

in the second line of Fig. 4). These diagrams depend on the bosonic transfer frequency/momentum $q = k_1 + k_3$ and one fermionic frequency $k = k_1$ or $k' = k_4$, respectively. The sum of such types of diagrams will be denoted as $\mathcal{K}_{2,pp}^{kq}$ and $\overline{\mathcal{K}}_{2,pp}^{k'q}$.

- Class 3: Every external frequency/momentum is attached to a different bare vertex. These diagrams depend independently on *all three* external arguments. Their sum will in the following be referred to as the “rest” function, denoted by $\mathcal{R}_{pp}^{kk'q}$. It is illustrated diagrammatically by the last diagram in the second row of Fig. 4.

Based on this classification, we can thus introduce an (a priori exact) decomposition of each reducible Φ -function into these four terms³. In the particle-particle channel it reads⁴

$$\Phi_{pp}^{kk'q} = \mathcal{K}_{1,pp}^q + \mathcal{K}_{2,pp}^{kq} + \overline{\mathcal{K}}_{2,pp}^{k'q} + \mathcal{R}_{pp}^{kk'q}. \quad (8)$$

In the same way we can decompose also the other scattering channels ph and \overline{ph} . It is important to note that the structures arising due to \mathcal{K}_1 , \mathcal{K}_2 and $\overline{\mathcal{K}}_2$ extend to infinitely large frequencies and, hence, generate a highly non-trivial high-frequency asymptotic behavior of the corresponding vertex function.

On the contrary, the diagrammatic content of \mathcal{R} implies a decay in all frequency directions, since each external fermionic frequency will enter directly one of the inner diagrammatic propagator lines by means of the frequency conservation at its attached bare vertex. These decay properties are verified numerically in Sec. V, and motivate our proposed approximation for treating the vertex asymptotics. Our strategy will be the following: We will explicitly consider the full frequency dependence of the Φ -functions only in a small frequency window, while the third class of diagrams (\mathcal{R}) will be neglected at larger frequencies, i.e.,

$$\Phi_{pp,\text{asympt.}}^{kk'q} \approx \mathcal{K}_{1,pp}^q + \mathcal{K}_{2,pp}^{kq} + \overline{\mathcal{K}}_{2,pp}^{k'q}. \quad (9)$$

One can see that the reducible vertex $\Phi_{pp}^{kk'q}$ is described by functions of *at most two* arguments in the asymptotic

³ Note that for \mathcal{K}_1 , \mathcal{K}_2 and $\overline{\mathcal{K}}_2$ respectively, the index denotes the reduced number of external arguments required to describe them. These shall in the following be referred to as ‘necessary’ arguments for the corresponding term.

⁴ Let us remark that the concrete form of the argument(s) for $\mathcal{K}_{1,pp}/\mathcal{K}_{2,pp}$ depend(s) on the chosen frequency/momentum convention. The dependence on one/two *single* argument(s) becomes apparent only in its natural notation, while for other conventions, $\mathcal{K}_{1,pp}/\mathcal{K}_{2,pp}$ will depend on one/two linear combination(s) of all frequencies/momenta. Nevertheless, these functions will be constant along two-dimensional planes/one-dimensional lines in the space of three frequencies/momenta (in the natural notation these planes/lines are parallel to the coordinate axes).

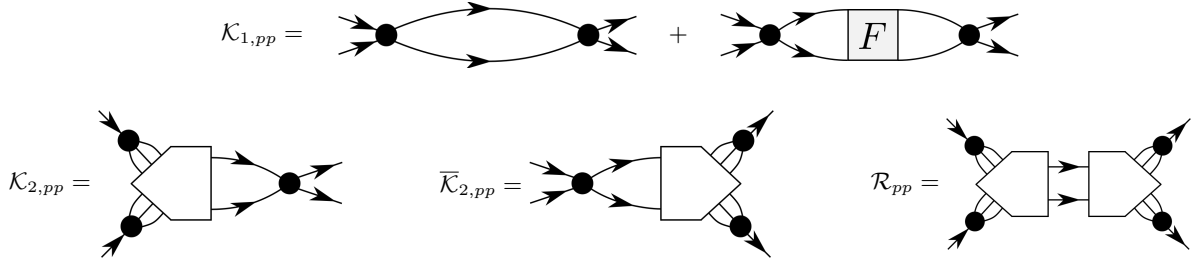


FIG. 4: Diagrammatic representation of the asymptotic functions for the particle-particle channel. For a more rigorous definition see Appendix C.

regime, which drastically lowers the cost for its numerical treatment. This way, we are able to (i) determine the reducible vertex Φ_{pp} up to arbitrarily large frequencies with a reduced computational effort, and (ii) avoid any problem arising from boundary effects due to finite-size frequency grids in vertex-based numerical algorithms.

Let us stress that, whenever momenta are considered, the decay of \mathcal{R} in the frequency domain implies that the reducible vertices Φ exhibit their full momentum dependence only in the domain of small frequencies. At larger frequency values, where the reducible vertex function is determined by at most two of the asymptotic functions, the momentum dependence is reduced alongside the frequencies. This matter will become evident in the following Sec. IV. The same argument holds for the fully irreducible vertex Λ_{2PI} , which decays to the value of the bare interaction in all frequency directions. As a consequence, strongly momentum dependent parts of the vertex F , e.g. the contributions responsible for a d -wave scattering amplitude, have to be localized in the frequency domain.

Let us now discuss the physical content of the asymptotic functions \mathcal{K}_1 and \mathcal{K}_2 . The former is directly linked to the susceptibility in the corresponding scattering channel^{3,4,7,18}. In fact, they are equal up to a prefactor U^2 , i.e.

$$\mathcal{K}_1^q = -U^2 \chi^q, \quad (10)$$

with χ^q defined according to Appendix A (compare Eqs. A8 and).

\mathcal{K}_2 on the other hand encodes information about how the electrons couple to different bosonic degrees of freedom. For instance, for the generalized density in Fourier space $n_q = \oint dk \sum_{\sigma} c_{\sigma}^{\dagger}(k) c_{\sigma}(k+q)$, we find the relation

$$U \times \langle \mathcal{T} n_q c_{\sigma}(k+q) c_{\sigma}^{\dagger}(k) \rangle_c = G_{\sigma}(k) G_{\sigma}(k+q) \sum_{\sigma'} \left(\mathcal{K}_{1,ph,\sigma\sigma'}^q + \mathcal{K}_{2,ph,\sigma\sigma'}^{kq} \right). \quad (11)$$

Here, $\langle \dots \rangle_c$ considers only connected contractions, and the imaginary time-ordering acts inside the Fourier integrals, and \oint denotes the generalized four-vector integration as introduced in Appendix A. The above equation identifies the sum of \mathcal{K}_1 and \mathcal{K}_2 with the expectation value $\langle \mathcal{T} n_q c_{\sigma}(k+q) c_{\sigma}^{\dagger}(k) \rangle_c$, which is directly related to

the electron-boson coupling (three-point or Hedin) vertex as used in the ladder version of DGA^{13,30} and the recently introduced TRILEX^{26,27} approach.

IV. IMPLEMENTATION

In this section, we describe how the ideas presented in the previous section can be practically exploited in analytical and numerical calculations based on two-particle vertex functions. After a general presentation of the main concepts, we will explicitly discuss the application of our scheme for analytic calculations based on the atomic limit vertex, and for numerical implementations of the fRG in its second order truncation and the parquet approximation.

The observation that any diagram vanishes if one of its necessary frequency arguments is taken to infinity allows us to select the different diagrammatic contributions by taking the corresponding limits in the frequency domain, i.e.

$$\lim_{|\nu| \rightarrow \infty} \lim_{|\nu'| \rightarrow \infty} \Phi_{r,\sigma\sigma'}^{kk'q} = \mathcal{K}_{1,r,\sigma\sigma'}^q, \quad (12a)$$

$$\lim_{|\nu'| \rightarrow \infty} \Phi_{r,\sigma\sigma'}^{kk'q} = \mathcal{K}_{1,r,\sigma\sigma'}^q + \mathcal{K}_{2,r,\sigma\sigma'}^{kq}, \quad (12b)$$

$$\lim_{|\nu| \rightarrow \infty} \Phi_{r,\sigma\sigma'}^{kk'q} = \mathcal{K}_{1,r,\sigma\sigma'}^q + \bar{\mathcal{K}}_{2,r,\sigma\sigma'}^{k'q}, \quad (12c)$$

where $r \in \{pp, ph, \bar{ph}\}$. We stress again the fact that, by taking limits in the frequency domain, we find alongside the reduced frequency dependence also a reduced momentum dependence. The remaining diagrammatic class 3 introduced in Sec. III, or rest function \mathcal{R} , which requires the full dependence on all arguments, can then be acquired by inverting Eq. (8)

$$\mathcal{R}_{r,\sigma\sigma'}^{kk'q} = \Phi_{r,\sigma\sigma'}^{kk'q} - \mathcal{K}_{1,r,\sigma\sigma'}^q - \mathcal{K}_{2,r,\sigma\sigma'}^{kq} - \bar{\mathcal{K}}_{2,r,\sigma\sigma'}^{k'q}. \quad (13)$$

One advantage of performing this limiting procedure based on the reducible vertex, is that Eq. (12a) holds equally if $|\nu|$ and $|\nu'|$ are taken to infinity at the same time, i.e.

$$\lim_{\substack{|\nu| \rightarrow \infty \\ |\nu'| \rightarrow \infty}} \Phi_{r,\sigma\sigma'}^{kk'q} = \mathcal{K}_{1,r,\sigma\sigma'}^q. \quad (14)$$

This property allows for a simplified scanning procedure to numerically extract asymptotic functions, which, depending on the frequency ranges and parameters, provide a good approximation.

The procedure is straightforward and applicable in all channels (see also Fig. 5 and Ref. 8):

- I: For large $|\nu|$ and $|\nu'|$ vary the transfer four-vector q to acquire \mathcal{K}_1^q .
- II: For large $|\nu'|$, vary k and the transfer four-vector q and subtract \mathcal{K}_1^q in order to obtain \mathcal{K}_2^{kq} .
- III: Repeat II by replacing $\nu' \rightarrow \nu$ and $k \rightarrow k'$ to determine $\bar{\mathcal{K}}_2^{k'q}$.

The above described procedure proposed to determine \mathcal{K}_1 and \mathcal{K}_2 has some limitations. Firstly, one can easily see that if the scanning is not performed at sufficiently large $|\nu|$ ($|\nu'|$), the rest function might not be fully decayed, giving rise to an error in the \mathcal{K}_1 and \mathcal{K}_2 extraction. We found this error to be particularly pronounced in the strong coupling regime ($U = 4$ for the comparisons in Sec. V) where the rest function becomes comparable with the asymptotic functions in the domain of small frequencies. Secondly, the scanning procedure requires the knowledge of the reducible vertex functions Φ_r , which are not directly available in some algorithms, as e.g. for the exact diagonalization. This raises the question whether a similar set of limits can be formulated also for F . And in fact, as will be clarified in the following, the limits

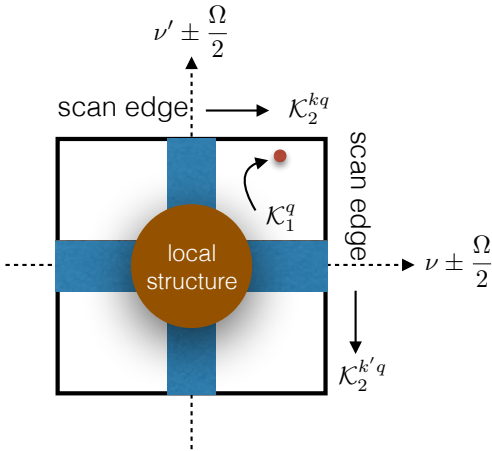


FIG. 5: Sketch of reducible vertex function in frequency space as a function of k and k' for fixed q , it consists of mainly two extensive stripes and a more dynamical structure locally centered at a position determined by the transfer frequency. The two stripes are described by $\mathcal{K}_{2,r}^{kq}$ and $\mathcal{K}_{2,r}^{k'q}$, the local structure is contained in the rest function \mathcal{R} . The nearly constant background is described by $\mathcal{K}_{1,r}^q$.

presented in Eq. (12) still hold, i.e.

$$\lim_{|\nu| \rightarrow \infty} \lim_{|\nu'| \rightarrow \infty} F_{r,\sigma\sigma'}^{kk'q} - (1 - \delta_{\sigma,\sigma'})U = \mathcal{K}_{1,r,\sigma\sigma'}^q, \quad (15a)$$

$$\lim_{|\nu'| \rightarrow \infty} F_{r,\sigma\sigma'}^{kk'q} - (1 - \delta_{\sigma,\sigma'})U = \mathcal{K}_{1,r,\sigma\sigma'}^q + \mathcal{K}_{2,r,\sigma\sigma'}^{kq}, \quad (15b)$$

$$\lim_{|\nu| \rightarrow \infty} F_{r,\sigma\sigma'}^{kk'q} - (1 - \delta_{\sigma,\sigma'})U = \mathcal{K}_{1,r,\sigma\sigma'}^q + \bar{\mathcal{K}}_{2,r,\sigma\sigma'}^{k'q}, \quad (15c)$$

where again F_r denotes the representation of F in one of the three mixed notations. However, the numerical equivalent of the limiting procedure, i.e. the scanning procedure previously described for the Φ -functions, is not feasible in the case of F , which is directly related to the fact that Eq. (14) does not hold equally for F . In order to numerically extract the asymptotics from F directly we thus suggest an alternative approach detailed in Appendix C. We implemented this diagrammatic extraction to determine the exact asymptotic functions, as presented in Sec. V, from ED calculations.

The limiting procedure Eq. (15) is however particularly suited in the case that analytical expressions for F are available, as demonstrated for the atomic limit case in Sec. IV A. Let us thus argue why this generalization of Eq. (12) holds. It relies on the property that any reducible diagram vanishes if the corresponding transfer frequency, being a necessary argument, is sufficiently large, i.e.

$$\lim_{|\Omega| \rightarrow \infty} \Phi_{r,\sigma\sigma'}^{kk'q} = 0. \quad (16)$$

We have to further consider, that in order to take the limits in Eq. (15), we should formulate Eq. (2) in the corresponding mixed notation. E.g. for the particle-particle channel we have to translate Φ_{ph} and $\Phi_{\bar{ph}}$ to the pp -notation as follows

$$F_{pp,\sigma\sigma'}^{kk'q} = \Phi_{pp,\sigma\sigma'}^{kk'q} + \Phi_{ph,\sigma\sigma'}^{kk'(q-k'-k)} + \Phi_{\bar{ph},\sigma\sigma'}^{k(q-k')(k'-k)} + \Lambda_{2PI,pp,\sigma\sigma'}^{kk'q}. \quad (17)$$

It now becomes clear that for fixed Ω and ν' , the bosonic frequencies of the ph and \bar{ph} channel, that is $\Omega - \nu' - \nu$ and $\nu' - \nu$, will lead to a vanishing of the respective scattering channels for $|\nu| \rightarrow \infty$. This behavior can also be observed in Fig. 1, and holds equally for the other scattering channels. Since Λ_{2PI} decays in all frequency directions to the bare interaction, we conclude that $\lim_{|\nu| \rightarrow \infty} F_{r,\sigma\sigma'}^{kk'q} - (1 - \delta_{\sigma,\sigma'})U = \lim_{|\nu| \rightarrow \infty} \Phi_{r,\sigma\sigma'}^{kk'q}$, while the same argument can be made for the other limits in Eq. (15).

A. The atomic limit

As a first showcase of these ideas we discuss the vertex decomposition for a system that can be treated analyti-

cally, i.e., the atomic limit, whose Hamiltonian reads

$$\hat{H} = U \left[\hat{n}_\uparrow \hat{n}_\downarrow - \frac{1}{2} (\hat{n}_\uparrow + \hat{n}_\downarrow) \right]. \quad (18)$$

Here, $\hat{n}_\sigma = \hat{c}_\sigma^\dagger \hat{c}_\sigma$ is the number operator for fermions of spin σ , and we have imposed the half-filling (particle-hole symmetry) condition $\mu = U/2$. The Hilbert space is spanned by the four eigenstates $|0\rangle$, $|\uparrow\rangle$, $|\downarrow\rangle$ and $|\uparrow\downarrow\rangle$, allowing for a direct calculation of the two-particle Green's functions by means of the Lehmann representation. The resulting two-particle vertex function^{4,5,31} is, for our purposes, split into four terms (note $\mathcal{F}_r \neq F_r$)

$$F_{\uparrow\downarrow} = \mathcal{F}_{\text{odd}} + \mathcal{F}_{pp} + \mathcal{F}_{ph} + \mathcal{F}_{\overline{ph}}, \quad (19)$$

which are defined in the following. The first term contains only odd orders in the interaction, and takes the most compact form in the purely fermionic notation

$$\mathcal{F}_{\text{odd}}^{\nu_1\nu_2\nu_3\nu_4} = U - \frac{U^3}{8} \frac{\sum_i \nu_i^2}{\prod_i \nu_i} - \frac{3U^5}{16} \prod_i \frac{1}{\nu_i}, \quad (20)$$

while the functions \mathcal{F}_r with $r \in \{pp, ph, \overline{ph}\}$ are more conveniently expressed in their respective mixed notation (see Appendix A)

$$\mathcal{F}_{pp}^{\nu\nu'\Omega} = -\beta \delta_{\Omega,0} \frac{U^2}{2} \mathcal{D}^{\nu\nu'} f\left(\frac{U}{2}\right), \quad (21a)$$

$$\mathcal{F}_{ph}^{\nu\nu'\Omega} = -\beta \delta_{\Omega,0} \frac{U^2}{4} \mathcal{D}^{\nu\nu'} \left[f\left(\frac{U}{2}\right) - f\left(-\frac{U}{2}\right) \right], \quad (21b)$$

$$\mathcal{F}_{\overline{ph}}^{\nu\nu'\Omega} = \beta \delta_{\Omega,0} \frac{U^2}{2} \mathcal{D}^{\nu\nu'} f\left(-\frac{U}{2}\right), \quad (21c)$$

with $\mathcal{D}^{\nu\nu'} = \frac{1}{\nu^2 \nu'^2} \left(\nu^2 + \frac{U^2}{4} \right) \left(\nu'^2 + \frac{U^2}{4} \right)$ and the Fermi function $f(\epsilon) = \frac{1}{1+e^{\beta\epsilon}}$. Note that, at this stage, the decomposition for the full vertex F is motivated solely by algebraic reasons, while the connection to the physical scattering channels will be established in the following.

Let us now use the limits in Eqs. (15) to identify the contributions arising from the different diagrammatic classes. This task can be performed by considering each term in Eq. (19) separately. Let us illustrate this procedure for the pp -channel, beginning with the first term, \mathcal{F}_{odd} . Here, we have to translate from the purely fermionic notation to the mixed pp -notation:

$$\begin{aligned} \mathcal{F}_{\text{odd},pp}^{\nu\nu'\Omega} &= \mathcal{F}_{\text{odd}}^{\nu,\Omega-\nu',\Omega-\nu,\nu'} = U - \frac{3U^5}{16} \frac{1}{\nu(\Omega-\nu')(\Omega-\nu)\nu'} \\ &\quad - \frac{U^3}{8} \frac{\nu^2 + (\Omega-\nu')^2 + (\Omega-\nu)^2 + \nu'^2}{\nu(\Omega-\nu')(\Omega-\nu)\nu'}. \end{aligned} \quad (22)$$

The large frequency limits then result in

$$\lim_{|\nu|\rightarrow\infty} \lim_{|\nu'|\rightarrow\infty} \mathcal{F}_{\text{odd},pp}^{\nu\nu'\Omega} = U, \quad (23a)$$

$$\lim_{|\nu'|\rightarrow\infty} \mathcal{F}_{\text{odd},pp}^{\nu\nu'\Omega} = U - \frac{U^3}{4} \frac{1}{\nu} \frac{1}{\nu - \Omega}, \quad (23b)$$

$$\lim_{|\nu|\rightarrow\infty} \mathcal{F}_{\text{odd},pp}^{\nu\nu'\Omega} = U - \frac{U^3}{4} \frac{1}{\nu'} \frac{1}{\nu' - \Omega}. \quad (23c)$$

As for the limits of the second term, \mathcal{F}_{pp} , we have

$$\lim_{|\nu|\rightarrow\infty} \lim_{|\nu'|\rightarrow\infty} \mathcal{F}_{pp}^{\nu\nu'\Omega} = -\beta \delta_{\Omega,0} \frac{U^2}{2} f\left(\frac{U}{2}\right), \quad (24a)$$

$$\lim_{|\nu'|\rightarrow\infty} \mathcal{F}_{pp}^{\nu\nu'\Omega} = -\beta \delta_{\Omega,0} \frac{U^2}{2} \left[1 + \frac{U^2}{4} \frac{1}{\nu^2} \right] f\left(\frac{U}{2}\right), \quad (24b)$$

$$\lim_{|\nu|\rightarrow\infty} \mathcal{F}_{pp}^{\nu\nu'\Omega} = -\beta \delta_{\Omega,0} \frac{U^2}{2} \left[1 + \frac{U^2}{4} \frac{1}{\nu'^2} \right] f\left(\frac{U}{2}\right). \quad (24c)$$

Determining the contributions from the remaining terms \mathcal{F}_{ph} and $\mathcal{F}_{\overline{ph}}$, which involves a translation from their respective mixed notation to the pp -notation, we find that their contributions vanish. This leads to the final expressions for the asymptotic functions in the pp -channel

$$\mathcal{K}_{1,pp,\uparrow\downarrow}^\Omega = -\beta \delta_{\Omega,0} \frac{U^2}{2} f\left(\frac{U}{2}\right), \quad (25a)$$

$$\mathcal{K}_{2,pp,\uparrow\downarrow}^{\nu\Omega} = \frac{U^2}{4} \frac{1}{\nu} \frac{1}{\nu - \Omega} (\mathcal{K}_{1,pp,\uparrow\downarrow}^\Omega - U), \quad (25b)$$

while the $\overline{\mathcal{K}}_2$ can be acquired by means of the symmetry properties reported in Appendix D. Performing the analogous procedure for the remaining two channels yields

$$\mathcal{K}_{1,ph,\uparrow\downarrow}^\Omega = -\beta \delta_{\Omega,0} \frac{U^2}{4} \left[f\left(\frac{U}{2}\right) - f\left(-\frac{U}{2}\right) \right], \quad (26a)$$

$$\mathcal{K}_{2,ph,\uparrow\downarrow}^{\nu\Omega} = \frac{U^2}{4} \frac{1}{\nu} \frac{1}{\nu + \Omega} (\mathcal{K}_{1,ph,\uparrow\downarrow}^\Omega - U), \quad (26b)$$

for the ph -channel, and

$$\mathcal{K}_{1,\overline{ph},\uparrow\downarrow}^\Omega = \beta \delta_{\Omega,0} \frac{U^2}{2} f\left(-\frac{U}{2}\right), \quad (27a)$$

$$\mathcal{K}_{2,\overline{ph},\uparrow\downarrow}^{\nu\Omega} = \frac{U^2}{4} \frac{1}{\nu} \frac{1}{\nu + \Omega} (\mathcal{K}_{1,\overline{ph},\uparrow\downarrow}^\Omega - U). \quad (27b)$$

in the \overline{ph} case.

Now that we have determined all asymptotic functions of the atomic limit vertex, let us consider its structures that are localized in the frequency domain. We proceed again in a term-wise fashion, beginning with \mathcal{F}_{odd} . By subtracting all asymptotic contributions arising from this term, we find that only the fifth order term $-\frac{3U^5}{16} \prod_i \frac{1}{\nu_i}$ survives, while it remains unclear whether this term can

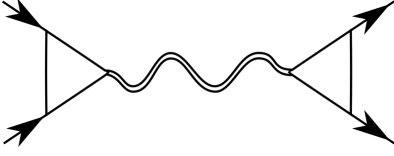


FIG. 6: Schematic diagrammatic representation of the localized structure presented in Eq. (28).

be attributed to the fully irreducible vertex function or the rest functions.

For the \mathcal{F}_r terms, let us again consider the pp -channel as an example. Here we find

$$\begin{aligned} \mathcal{F}_{pp}^{\nu\nu'\Omega} &= \lim_{|\nu'|\rightarrow\infty} \mathcal{F}_{pp}^{\nu\nu'\Omega} - \lim_{|\nu|\rightarrow\infty} \mathcal{F}_{pp}^{\nu\nu'\Omega} + \lim_{|\nu|\rightarrow\infty} \lim_{|\nu'|\rightarrow\infty} \mathcal{F}_{pp}^{\nu\nu'\Omega} \\ &= \left(\frac{U^2}{4} \frac{1}{\nu} \frac{1}{\nu - \Omega} \right) \times \mathcal{K}_{1,pp,\uparrow\downarrow}^\Omega \times \left(\frac{U^2}{4} \frac{1}{\nu'} \frac{1}{\nu' - \Omega} \right). \end{aligned} \quad (28)$$

This term contains three factors, i.e. a fermion-boson vertex²⁸ that describes the coupling to a pairing field, the bosonic propagator in the pp -channel, and an additional fermion-boson vertex, as depicted schematically in Fig. 6. We can thus argue diagrammatically that this localized term belongs to the rest function $\mathcal{R}_{pp,\uparrow\downarrow}$. For the other channels, we find equally that the localized structures belong to the respective rest function, and hence $\mathcal{F}_r \in \Phi_{r,\uparrow\downarrow}$.

Note that, to obtain the full rest functions as well as the fully irreducible vertex function, it would require the analytic expressions for all the reducible Φ functions, that have so far never been reported in the literature. Their calculation requires the very involved procedure of inverting analytically the Bethe-Salpeter equations, which goes beyond the scope of this paper. The resulting expressions should reproduce the multiple vertex divergencies^{32–35} appearing in the Φ functions for $T \leq \frac{\sqrt{3}}{2\pi}U$. As these divergent terms are not present in the full vertex F , they must be subjected to cancellations between $\Lambda_{2\text{PI}}$ and one (or more) of rest functions.

B. Implementation for the fRG solver

The functional renormalization group approach^{9,36} implements Wilson's renormalization group idea in a general field-theoretical framework. By introducing a scale-dependence into the quadratic part of the action, i.e. the non-interacting propagator

$$G_0(i\nu) \rightarrow G_0^\Lambda(i\nu),$$

one can derive an exact functional flow equation³⁷ for the 1PI generating functional, also named "effective ac-

tion". This flow equation describes the gradual evolution of all correlation functions as the scale Λ is varied from the initial to the final value. Being an exact reformulation of the initial problem, it serves as a basis for further approximations, and has been used in many different applications ranging from high-energy physics to condensed matter theory. In the fRG, this approximation consists in an expansion in orders of the fields, resulting in an infinite hierarchy of coupled ordinary differential equations for all 1PI n -particle vertex functions, e.g. the self-energy Σ , the two-particle vertex F and so on. This hierarchy is typically truncated at the two-particle level, rendering the fRG perturbative in the interaction strength³⁸.

For the flow-parameter dependence, we consider in the following two different schemes: The so-called Ω -flow³⁹:

$$G_0^\Lambda(i\nu) = \frac{\nu^2}{\nu^2 + \Lambda^2} G_0(i\nu), \quad (29)$$

and the U -flow⁴⁰:

$$G_0^\Lambda(i\nu) = \Lambda \cdot G_0(i\nu). \quad (30)$$

The Ω -flow introduces an energy cutoff into the system, that allows to successively integrate out the different energy scales from high to low. This approach is very much in the spirit of other renormalization group approaches. The U -flow on the other hand introduces a frequency-independent regulator into the Green function that treats all energy scales on a equal footing. In this sense, the U -flow is more similar to common perturbative approaches.

The flow-equations resulting from a second order truncation of the flow-equation hierarchy can be summarized as follows, where, for simplicity, we consider the $SU(2)$ symmetric case. At the level of the self-energy, the derivative takes the simple form

$$\dot{\Sigma}(k)^\Lambda = \oint dk' S^\Lambda(k') \times \left[F_{ph,\uparrow\downarrow}^{\Lambda,kk'(q=0)} + F_{ph,\uparrow\uparrow}^{\Lambda,kk'(q=0)} \right], \quad (31)$$

where we have introduced the so-called single-scale propagator

$$S^\Lambda(i\nu) = \partial_\Lambda G^\Lambda(i\nu)|_{\Sigma^\Lambda \text{ fixed}}.$$

At the level of the 1PI two-particle vertex, the flow-equation is composed of contributions from three scattering channels (particle-particle, particle-hole and transverse particle-hole)

$$\dot{F}^\Lambda = \mathcal{T}_{pp}^\Lambda + \mathcal{T}_{ph}^\Lambda + \mathcal{T}_{ph}^\Lambda, \quad (32)$$

where

$$\mathcal{T}_{pp,\uparrow\downarrow}^{\Lambda,kk'q} = \oint dk'' \left[S^\Lambda(k'') G^\Lambda(q - k'') + S \leftrightarrow G \right] \times F_{pp,\uparrow\downarrow}^{\Lambda,qk''} F_{pp,\uparrow\downarrow}^{\Lambda,qk''k'}, \quad (33a)$$

$$\mathcal{T}_{ph,\uparrow\downarrow}^{\Lambda,kk'q} = - \oint dk'' \left[S^\Lambda(k'' + q) G^\Lambda(k'') + S \leftrightarrow G \right] \times \left[F_{ph,\uparrow\uparrow}^{\Lambda,kk''q} F_{ph,\uparrow\downarrow}^{\Lambda,k''k'q} + F_{\uparrow\uparrow} \leftrightarrow F_{\uparrow\downarrow} \right], \quad (33b)$$

$$\mathcal{T}_{ph,\uparrow\downarrow}^{\Lambda,kk'q} = \oint dk'' \left[S^\Lambda(k'' + q) G^\Lambda(k'') + S \leftrightarrow G \right] \times F_{ph,\uparrow\downarrow}^{\Lambda,kk''q} F_{ph,\uparrow\downarrow}^{\Lambda,k''k'q}. \quad (33c)$$

These terms can be depicted diagrammatically as shown in Fig. 7 for the pp -channel. To understand the diagrammatic content generated by each channel let us refer to the previously introduced parquet equation, that holds for any scale Λ

$$F^\Lambda = \Lambda_{2\text{PI}}^\Lambda + \Phi_{pp}^\Lambda + \Phi_{ph}^\Lambda + \Phi_{ph}^\Lambda. \quad (34)$$

Considering the vertex flow equation Eq. (32) (see also Fig. 7), it is obvious that at this level of truncation, the only diagrammatic content that can be generated by the flow is two-particle reducible, meaning $\Lambda_{2\text{PI}}^\Lambda = \bar{\Lambda}_{2\text{PI}}^{\Lambda_{\text{ini}}}$. We can thus separate the different two-particle reducible terms in Eq. (32), and identify

$$\dot{\Phi}_{pp}^\Lambda = \mathcal{T}_{pp}, \quad \dot{\Phi}_{ph}^\Lambda = \mathcal{T}_{ph}, \quad \dot{\Phi}_{ph}^\Lambda = \mathcal{T}_{ph}. \quad (35)$$

This allows us to make use of the parametrization scheme described in Sec. III during the fRG flow. While keeping track of the reducible vertex functions on a finite frequency grid, we also track the flow of the previously introduced asymptotic functions. In fact, we can directly perform the limits in Eq. (12) to compute the corresponding derivatives

$$\dot{\mathcal{K}}_{1,r,\sigma\sigma'}^{\Lambda,q} = \lim_{|\nu| \rightarrow \infty} \lim_{|\nu'| \rightarrow \infty} \dot{\Phi}_{r,\sigma\sigma'}^{\Lambda,kk'q}, \quad (36a)$$

$$\dot{\mathcal{K}}_{2,r,\sigma\sigma'}^{\Lambda,kq} = \lim_{|\nu'| \rightarrow \infty} \dot{\Phi}_{r,\sigma\sigma'}^{\Lambda,kk'q} - \dot{\mathcal{K}}_{1,r,\sigma\sigma'}^{\Lambda,q}, \quad (36b)$$

$$\dot{\mathcal{K}}_{2,r,\sigma\sigma'}^{\Lambda,k'q} = \lim_{|\nu| \rightarrow \infty} \dot{\Phi}_{r,\sigma\sigma'}^{\Lambda,kk'q} - \dot{\mathcal{K}}_{1,r,\sigma\sigma'}^{\Lambda,q}. \quad (36c)$$

In practice, these limits are performed numerically by setting the corresponding frequency to an arbitrarily large value. In doing this, we have to determine F^Λ in the large frequency domain by making use of Eq. (9). In addition to the flow of the Φ -functions we then track, using Eqs. (36), the flow of the asymptotic functions.

Due to the numerical costs involved in treating the full argument dependence of the vertex function, a simplified

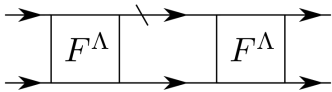


FIG. 7: Diagrammatic representation of the particle-particle contribution \mathcal{T}_{pp} (33a) in the vertex flow equation. The dashed line denotes the single-scale propagator S^Λ .

parametrization scheme⁴¹

$$\Phi_{pp}^{kk'q} \approx \mathcal{K}_{\text{eff},pp}^q = \mathcal{K}_{1,pp}^q + \mathcal{K}_{2,pp}^{([\Omega/2] - \nu_0, \mathbf{k})q} + \bar{\mathcal{K}}_{2,pp}^{([\Omega/2] - \nu_0, \mathbf{k}')q} + \mathcal{R}_{pp}^{([\Omega/2] - \nu_0, \mathbf{k})([\Omega/2] - \nu_0, \mathbf{k}')q} \quad (37)$$

has found extensive use in the fRG community. Here, $\nu_0 = \frac{\pi}{\beta}$ denotes the first positive Matsubara frequency, and $[\dots]$ will round up to the next bosonic Matsubara frequency⁵. This scheme considers only the dominant transfer frequency dependence of the \mathcal{K}_2 and \mathcal{R} functions, and will be compared to the full parametrization in Sec. V 3. Performing the same approximation in the momentum domain limits the scattering to the s-wave type, while higher harmonics can be captured by means of a form-factor expansion⁴².

The fRG flow equations in their second order truncated form account for the feedback of F^Λ into the flow up to the second order. If we in addition consider partially the neglected contribution of the 1PI three-particle vertex in the flow equations, it is possible to account fully for the feedback up to $\mathcal{O}[(F^\Lambda)^3]$. In practice this is achieved by taking into account both self-energy⁶, and vertex corrections from diagrams with overlapping loops^{43,44}, which is possible with a manageable numerical effort⁴⁴. These corrections will in the following be referred to as two-loop (2ℓ) corrections to distinguish this scheme from the conventional one-loop (1ℓ) one.

When considering the flow of the asymptotic functions, we find that including the two-loop corrections gives a substantial improvement of the two-particle vertex results. While a quantitative comparison between the one- and two-loop scheme will be presented in Sec. V 2, we can already understand from a simple diagrammatic argument that the lowest order contribution to \mathcal{K}_2 is not fully captured in the one-loop scheme. Here, the derivative includes four contributions, as depicted in Fig. 8.

⁵ The parametrization scheme presented in Eq. (37) was originally implemented at zero temperature, where the flow of each channel was determined for vanishing transfer frequency of the other two channels. At finite temperature, this choice is only possible for every other transfer frequency, as the condition $\left(\frac{\beta}{2\pi} \sum_r \Omega_r\right) \bmod 2 = 1$ needs to hold. This leads to ambiguities in the definition.

⁶ The self-energy correction $S \rightarrow \partial_\Lambda G^\Lambda$ is generally referred to as Katanin-substitution⁴³.

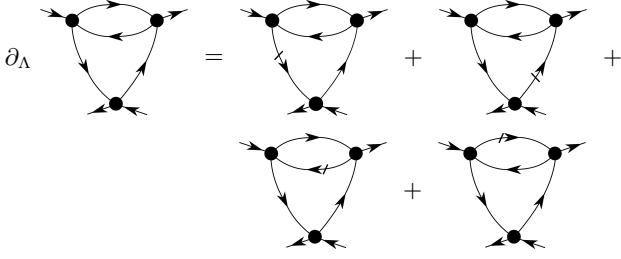


FIG. 8: Derivative of the lowest order contribution to $\mathcal{K}_{2,ph}^\Lambda$.

The one-loop scheme accounts only for the first two diagrams, while the two-loop scheme includes all of them. In particular for the U -flow, the contribution from all four diagrams is equal, meaning that in its one-loop implementation the flow reproduces exactly $\frac{1}{2}$ of the exact value for $U \rightarrow 0$. This is verified numerically in Sec. V 2 (see Fig. 20). A similar argument can be made for the lowest order diagram of \mathcal{R} , where the resulting factor is $\frac{1}{3}$.

C. Implementation for the parquet solver

In this section we discuss the implications of the asymptotic functions \mathcal{K}_1^q and \mathcal{K}_2^{kq} in the context of the parquet equations, that have been previously addressed from a numerical perspective⁷ in Ref. 8. We further demonstrate how the diagrams of \mathcal{K}_1 , \mathcal{K}_2 and \mathcal{R} emerge naturally in a self-consistent solution of the parquet approximation.

Given the fully irreducible vertex function $\Lambda_{2\text{PI}}$, the parquet equations¹ form a closed set of equations for the vertex functions F , Γ_r and Φ_r as well as the self-energy Σ . They can be summarized schematically as

$$F = \Lambda_{2\text{PI}} + \sum_r \Phi_r \quad \Gamma_r = \Lambda_{2\text{PI}} + \sum_{r' \neq r} \Phi_{r'} \quad (38a)$$

$$\Phi_r = \Gamma_r G G F \quad \Sigma = U \cdot G G G \cdot F, \quad (38b)$$

while the detailed explicit forms of these equations are presented in Appendix B.

In the following we consider the $SU(2)$ symmetric case, which allows us to decouple the Bethe-Salpeter equations by introducing the density (d), magnetic (m), singlet (s) and triplet (t) channel

$$\Phi_d = \Phi_{ph,\uparrow\uparrow} + \Phi_{ph,\uparrow\downarrow} \quad \Phi_m = \Phi_{ph,\uparrow\uparrow} - \Phi_{ph,\uparrow\downarrow}, \quad (39a)$$

$$\Psi_s = \Phi_{pp,\uparrow\downarrow} - \Phi_{pp,\uparrow\uparrow} \quad \Psi_t = \Phi_{pp,\uparrow\downarrow} + \Phi_{pp,\uparrow\uparrow}, \quad (39b)$$

and F_r , Γ_r , \mathcal{R}_r , $\mathcal{K}_{1,r}$ and $\mathcal{K}_{2,r}$ for $r \in \{d, m, s, t\}$ are defined in the same way.

⁷ We note that the 'Kernel functions' Φ_r^q and Φ_r^{qk} introduced in Ref. 8 are related to \mathcal{K}_1 and \mathcal{K}_2 as $\Phi_r^q = \mathcal{K}_{1,r}^q$ and $\Phi_r^{qk} = \mathcal{K}_{1,r}^q + \mathcal{K}_{2,r}^{kq}$.

As observed in Ref. 8 and detailed in the previous sections, the reducible two-particle vertices Φ_r play a fundamental role in the correct treatment of the two-particle vertex function F , and thus for the solution of the parquet equations. The closed set of equations (38) is solved self-consistently by using the iterative procedure described in the following. For this solution of the parquet equations, the fact that the asymptotic functions \mathcal{K}_1 and \mathcal{K}_2 allow us to determine the vertex functions on the whole frequency domain is essential, as every step of the solution requires translations between the different notations as e.g. demonstrated in Eq. (17). If the vertex functions were known only on a finite frequency grid, these translations would lead to a loss of frequencies with every iteration of the parquet equations.

The only approximation that enters in the solution of the parquet equations is the choice of the fully irreducible vertex $\Lambda_{2\text{PI}}$. In the parquet approximation, it is approximated by its lowest order contribution $\Lambda_{2\text{PI}} \sim U$, while the DGA^{8,13,45} approximates $\Lambda_{2\text{PI}}$ by the local one of the effective impurity model. A typical procedure for the solution of the parquet approximation can then be outlined as follows:

1. Choose a finite but sufficiently large frequency range $[-\lambda, \lambda]$ for the problem studied
2. Initialize Σ and the vertex functions Φ_r to 0, or make some educated guess for their starting values. Initialize F and Γ_r according to Eq. (38a).
3. Calculate the reducible vertex functions $\Phi_r^{kk'q}$ with frequency arguments in the range $[-\lambda, \lambda]$ from the Bethe-Salpeter equations [Eq. (38b) left].
4. Determine the asymptotic functions using

$$\mathcal{K}_{1,r}^q = \lim_{|\nu| \rightarrow \infty} \lim_{|\nu'| \rightarrow \infty} \Phi_r^{kk'q},$$

$$\mathcal{K}_{2,r}^{kq} = \lim_{|\nu'| \rightarrow \infty} \Phi_r^{kk'q} - \mathcal{K}_{1,r}^q,$$

where the limits are performed numerically using the Bethe-Salpeter equations. For an implementation using the scanning procedure outlined in Sec. IV, see Ref. 8.

5. Compute the vertex functions $F_r^{kk'q}$ and $\Gamma_r^{kk'q}$ using the updated values of $\Phi_r^{kk'q}$ [Eq. (38a)]. When any of the three frequency arguments of k, k' or q fall outside of the range $[-\lambda, \lambda]$, we approximate

$$\Phi_{pp, \text{asympt.}}^{kk'q} \approx \mathcal{K}_{1,pp}^q + \mathcal{K}_{2,pp}^{kq} + \bar{\mathcal{K}}_{2,pp}^{k'q}.$$

6. Calculate the self-energy from F through the Schwinger-Dyson equation [Eq. (38b) right].
7. Go back to step 3 and iterate until convergence is achieved.

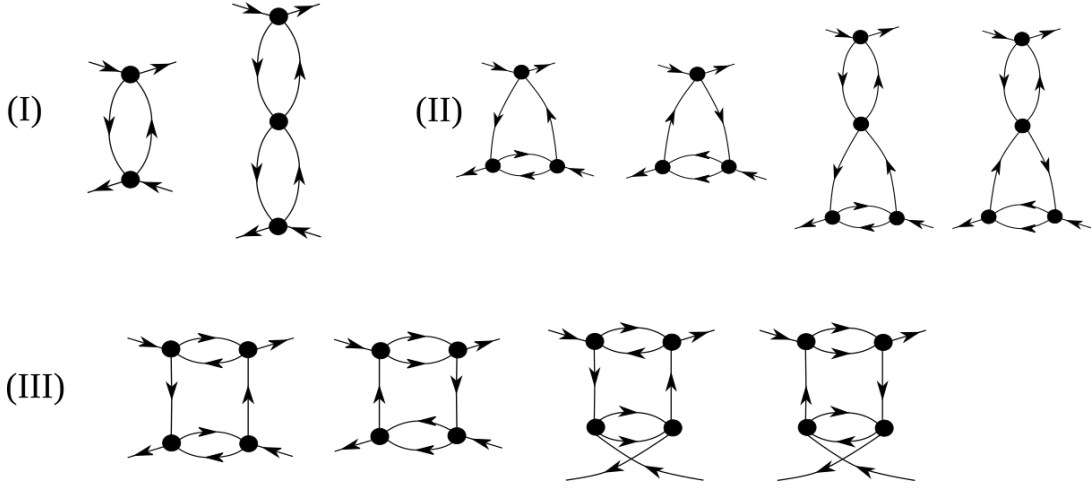


FIG. 9: Part of the Feynman diagrams for the reducible vertex function $\Phi_d^{kk'q}$ generated in the first two iterations of a parquet approximation calculation. The diagrams can be attributed to (I) $\mathcal{K}_{1,d}^q$, (II) $\mathcal{K}_{2,d}^{kq}$ and (III) $\mathcal{R}_d^{kk'q}$ respectively.

Let us now consider diagrams (see Fig. 9 for the d -channel) generated in the first iterations of the parquet approximation solution (assuming initial conditions $\Phi_r = 0$), and attribute them to the diagrammatic classes I (\mathcal{K}_1), II ($\mathcal{K}_2, \bar{\mathcal{K}}_2$) and III (\mathcal{R}). After the first iteration the reducible vertex functions $\Phi_r^{kk'q}$ read

$$\Phi_d^{kk'q} = U^2 \chi_{0,ph}^q \quad \Phi_m^{kk'q} = U^2 \chi_{0,ph}^q, \quad (40a)$$

$$\Psi_s^{kk'q} = -2U^2 \chi_{0,pp}^q \quad \Psi_t^{kk'q} = 0, \quad (40b)$$

where χ_0 denotes the non-interacting bubble (see first diagram in Fig. 9 for the d case). This corresponds to the lowest order perturbation theory for Φ_r , which is only dependent on the transfer frequency and momentum q , and can thus be attributed to $\mathcal{K}_{1,r}$. The dependence of Φ on the fermionic arguments is only generated when the updated vertex functions F and Γ , e.g. for the d -channel

$$F_d^{kk'q} = U - 2U^2 \chi_{0,ph}^{k'-k} - U^2 \chi_{0,pp}^{k+k'+q} + U^2 \chi_{0,ph}^q, \quad (41a)$$

$$\Gamma_d^{kk'q} = U - 2U^2 \chi_{0,ph}^{k'-k} - U^2 \chi_{0,pp}^{k+k'+q}, \quad (41b)$$

are inserted into the Bethe-Salpeter equation in the second iteration. This produces the remaining diagrams in Fig. 9, and thus the first contributions to the \mathcal{K}_2 (II) and \mathcal{R} (III) functions. Iterating this procedure, we generate successively all reducible diagrams. Results obtained by this approach for a SIAM are presented in the following Sec. V.

V. COMPARISON TO EXACT RESULTS OF THE SIAM

In this section we illustrate the high quality of the description of the vertex asymptotics obtained using the algorithmic implementations discussed in the previous sections.

In particular, we present results for the asymptotic functions as obtained from the fRG (Ω -flow including two-loop corrections) and parquet approximation for a single impurity Anderson model and compare them with exact diagonalization data, which were acquired following the procedure outlined in Appendix C. Besides the asymptotic functions, also results for the rest function and the self-energy will be shown. In Sec. V 2 we will further discuss a detailed comparison between the fRG in its one- and two-loop implementation for both the Ω - as well as the U -flow. We first consider the regime of weak coupling where the fRG and the PA, as approximation schemes, are expected to be quantitatively correct. Hence, in this regime, the comparison with the exact results of ED will represent a stringent test for our treatment of the high-frequency asymptotics. After having demonstrated that the error introduced in the high-frequency asymptotics of the vertex function is negligible, we proceed by applying our fRG and PA algorithms, including the high-frequency treatment, to the intermediate to strong coupling regime. In this case, the comparison to the ED will allow us to assess directly the intrinsic performance of the two approximations in the non-perturbative parameter region, because no spurious effects are introduced by an incorrect treatment of the high-frequency part anymore.

The system of interest in this section is a SIAM, i.e. a single impurity site with local repulsive Coulomb interaction U coupled to a non-interacting bath (see Sec. II, Eq. (1)). In our specific case, we consider a box-like density of states

$$\rho(\omega) = \frac{1}{2D} \Theta(D - |\omega|), \quad (42)$$

where D denotes the half-bandwidth, which will be used as our unit of energy, i.e. $D = 1$. This bath is coupled to our impurity site by means of a hopping $t = \sqrt{2}/\pi$, such

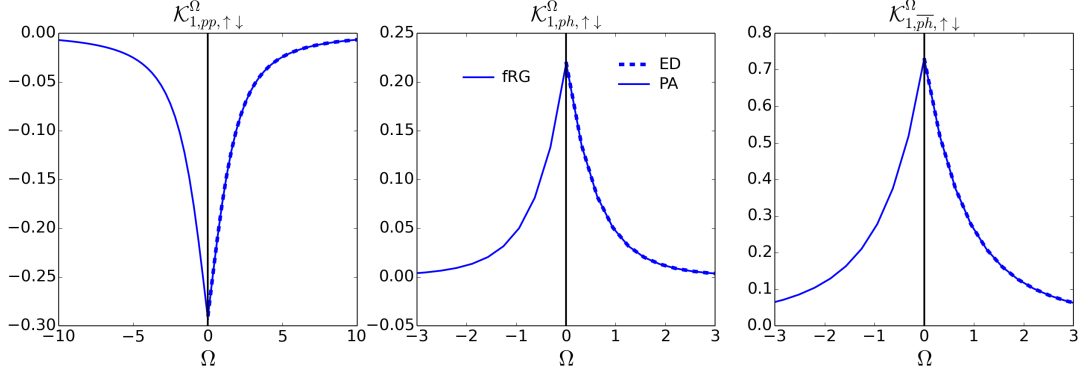


FIG. 10: $\mathcal{K}_{1,\uparrow\downarrow}^\Omega$ for all three scattering channels. We present results obtained by fRG (left, solid), PA (right, solid) and ED (right, dashed) for the SIAM with $U = 1$, $\beta = 20$ and $\Delta(0) = D = 1$.

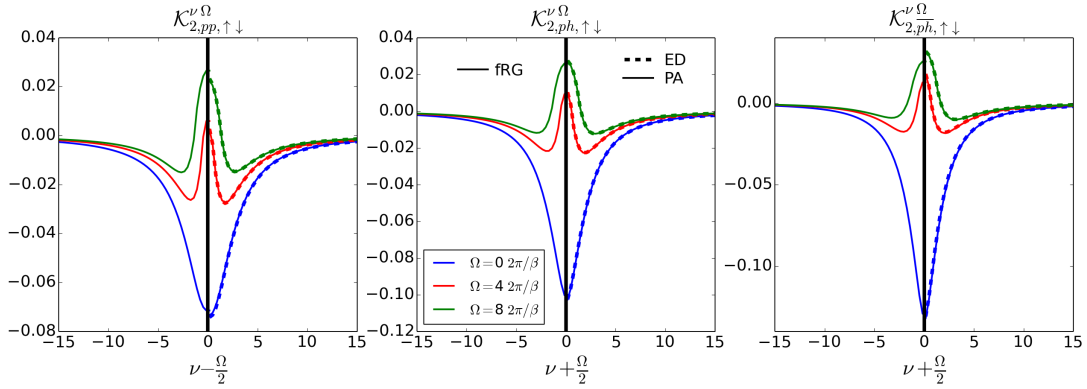


FIG. 11: $\mathcal{K}_{2,\uparrow\downarrow}^{\nu\Omega}$ for all three scattering channels as a function of ν and for different values of Ω . We present results obtained by fRG (left, solid), PA (right, solid) and ED (right, dashed) for the SIAM with $U = 1$, $\beta = 20$ and $\Delta(0) = D = 1$.

that the resulting hybridization function reads $\Delta(\omega) = \pi t^2 \rho(\omega) = 2\rho(\omega)$. This choice results in $\Delta(0) = D = 1$, allowing us to directly relate our unit of energy to the one used in wide-band limit calculations⁴¹, namely the hybridization function evaluated at the chemical potential.

However, the exact diagonalization of the SIAM is not possible for $\rho(\omega)$ of Eq. (42). Hence, we have determined a set of four optimized bath energy levels ϵ_n and hoppings t_n with the resulting hybridization function

$$\Delta^{\text{ED}}(i\nu) = \sum_{n=1}^4 \frac{t_n^2}{i\nu - \epsilon_n}, \quad (43)$$

in order to mimic the continuous bath of Eq. (42) in the best way possible within a discretized ED scheme. Following a somewhat similar strategy as in the ED algorithms for DMFT, we determine our bath parameters such that the norm

$$\sum_{i\nu} |\Delta^{\text{ED}}(i\nu) - \Delta(i\nu)|^2 \quad (44)$$

is minimized. For an inverse temperature $\beta = 20$, which was used for all numerical calculations presented in this

paper, we have $\epsilon_n = -0.7, -0.15, 0.15, 0.7$ and $t_n = 0.45, 0.34, 0.34, 0.45$. Note also that, since we are considering the particle-hole symmetric case, all two-particle quantities are purely real, while the self-energy is purely imaginary. Unless mentioned otherwise, calculations are performed with a frequency grid of $128 \times 128 \times 256$ Matsubara frequencies for the Φ -functions, while grids of 128×256 and 256 are chosen for \mathcal{K}_2 and \mathcal{K}_1 respectively.

Let us start considering the weak-coupling case ($U = 1$). The data for $\mathcal{K}_{1,\uparrow\downarrow}$, $\mathcal{K}_{2,\uparrow\downarrow}$ and $\mathcal{R}_{\uparrow\downarrow}$ are presented in Fig. 10, Fig. 11 and Figs. 12 and 13 respectively⁸. For this parameter choice, we find an excellent agreement between the different approaches and the exact solution for all quantities. At the level of the asymptotic function $\mathcal{K}_{1,\uparrow\downarrow}$, no distinction can be made between the results of the different schemes, while for $\mathcal{K}_{2,\uparrow\downarrow}$ the fRG shows some minor deviations w.r.t. PA and ED in the pp and

⁸ The contour plots are created such that every small square of equal color represents the value of the function at the bottom left corner of this square.

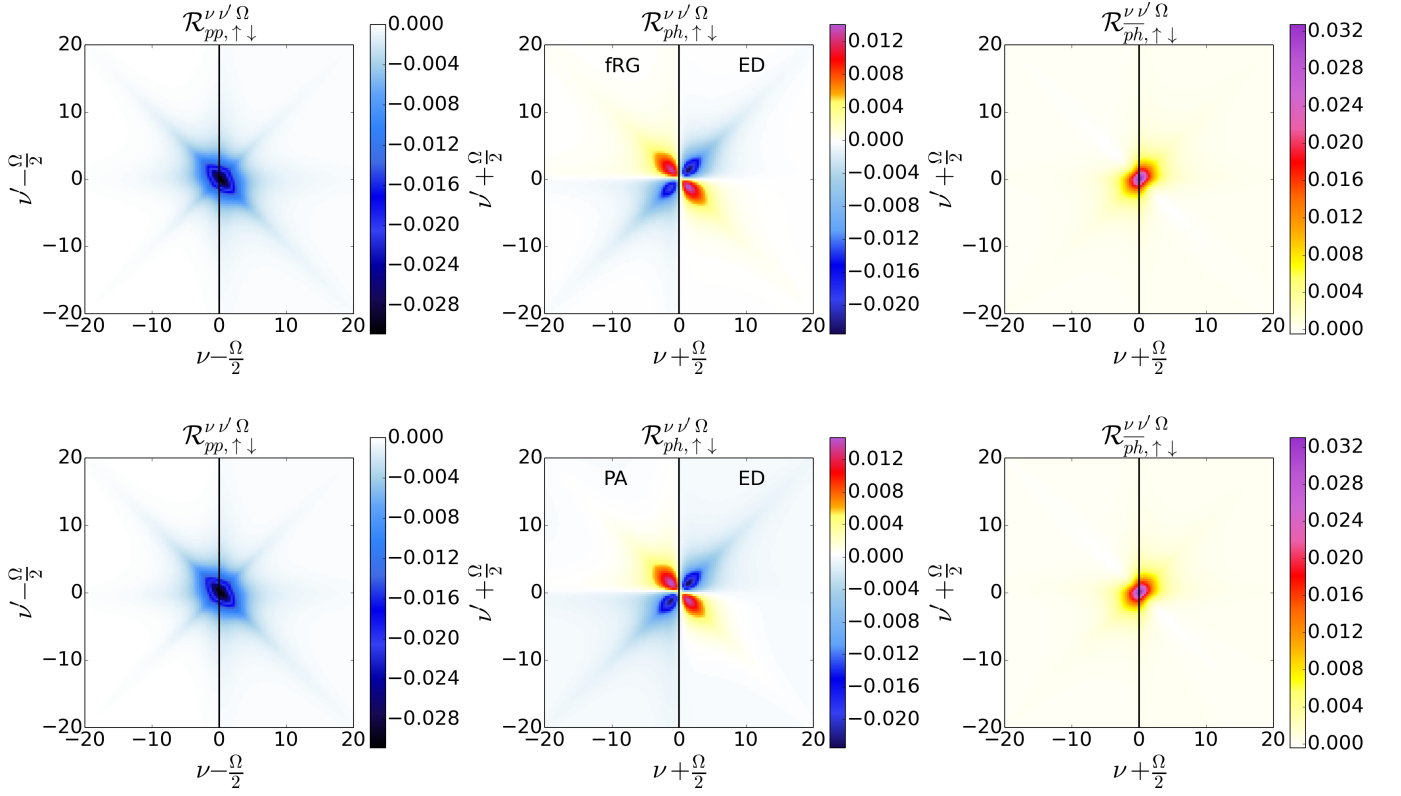


FIG. 12: Rest function $\mathcal{R}_{\uparrow\downarrow}^{\nu\nu'\Omega}$ for all three scattering channels as a function of ν and ν' plotted for $\Omega = 0$. We present results obtained by fRG (1st row, left) and PA (2nd row, left) for the SIAM with $U = 1$, $\beta = 20$ and $\Delta(0) = D = 1$. The right side always shows the corresponding ED result.

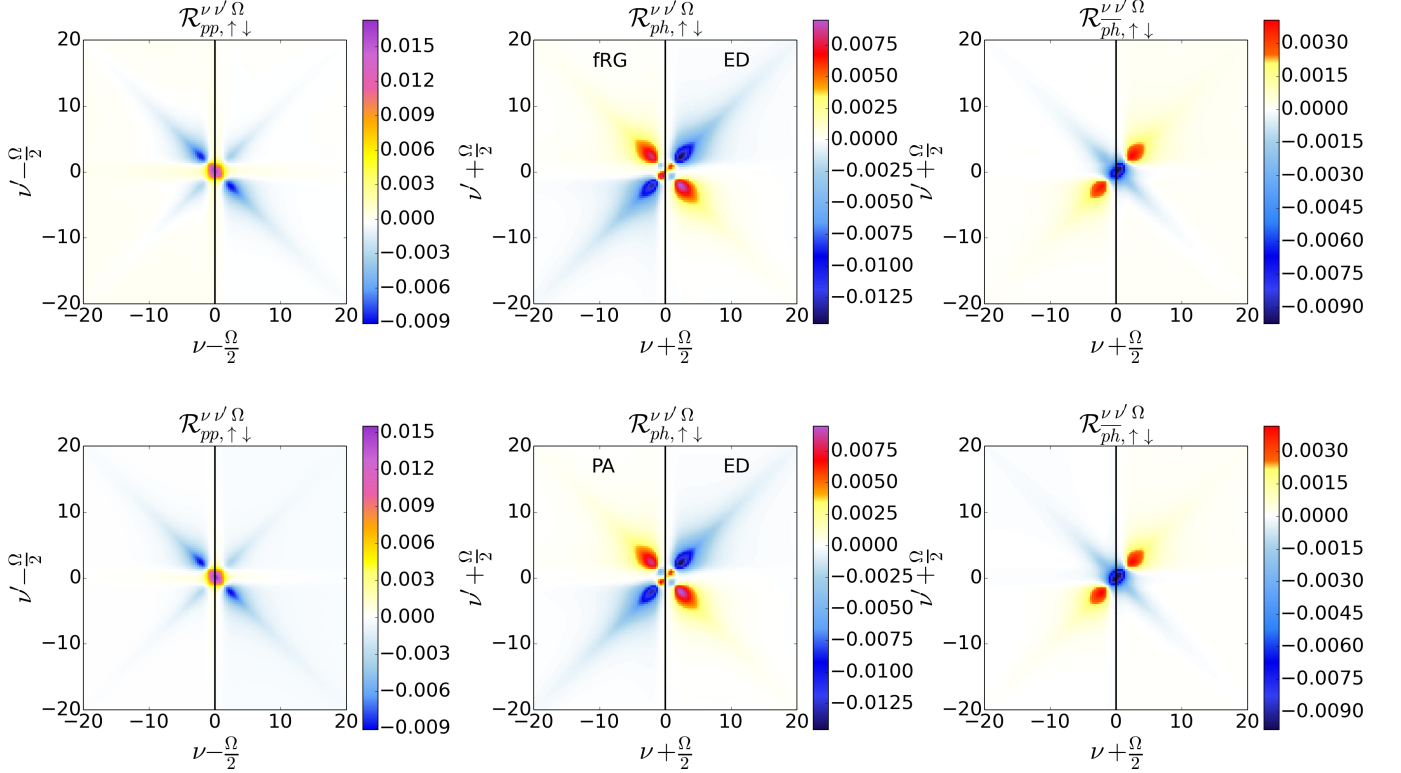


FIG. 13: Same as Fig. 12, but for a finite transfer frequency $\Omega = 8 \frac{2\pi}{\beta}$.

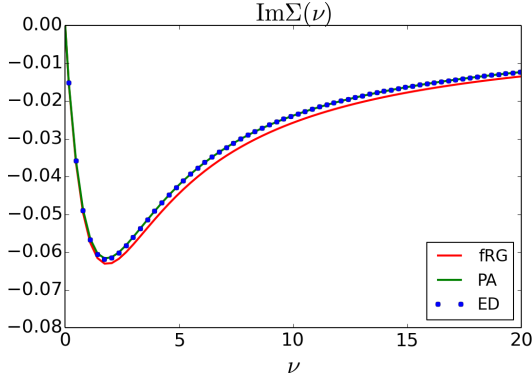


FIG. 14: $\text{Im}\Sigma(i\nu)$ as obtained by fRG (red, solid), PA (green, solid) and ED (blue, dotted) for the SIAM with $U = 1$, $\beta = 20$ and $\Delta(0) = D = 1$.

\overline{ph} channel. Even at the level of the rest function $\mathcal{R}_{\uparrow\downarrow}$, which has as a leading order U^4 , we find excellent agreement between PA and ED, while only minor deviations are again observed for the fRG. Note that, contrary to the plotting conventions adopted in previous Refs. 4,8, the fermionic frequencies are shifted by $\pm\Omega/2$ for \mathcal{K}_2 and \mathcal{R} , because the main frequency structures move outwards as Ω is increased. This observation suggests to include a corresponding shift also in the notation used in the numerical implementation, such that the localized frequency structures can be more efficiently captured by means of the finite grid even in the case of finite transfer frequency. Similar trends are observed for the self-energy shown in Fig. 14. While PA and ED agree perfectly, we find that the fRG self-energy deviates from the exact results, especially in its tail.

All this numerical evidence proves the reliability of our treatment of the high frequency asymptotics within the different schemes (see also the results for $U = 2$ in the supplements), allowing us to evaluate in an unbiased way their intrinsic performance in the most challenging strong-coupling regime.

Due to the perturbative nature of fRG and PA, the situation changes drastically in the regime of stronger coupling. The corresponding results for $U = 4$ are presented for $\mathcal{K}_{1,\uparrow\downarrow}$ and $\mathcal{K}_{2,\uparrow\downarrow}$ in Figs. 15 and 16 respectively. Note that, for this value of the interaction, we are clearly in the non-perturbative regime, as divergencies^{32–34,46,47} are already present in the exact vertices obtained by ED.

For both, PA and fRG, $\mathcal{K}_{1,\uparrow\downarrow}$ shows already strong deviations from the exact results, while the qualitative structures are still captured. These deviations are particularly enhanced in the ph and \overline{ph} channel. In the case of $\mathcal{K}_{2,\uparrow\downarrow}$ qualitative features are missed by the PA and fRG, in particular for $\Omega = 0$, while a qualitative agreement is still achieved for finite transfer frequency. As the main structures of the rest function \mathcal{R} are neither reproduced by PA nor by fRG, we show only one example for this comparison in Fig. 17 (the full vertices are reported in the supplements). Since this diagrammatic class is at

least fourth order in the interaction, the strongest deviations were to be expected here. Finally, we note that for the self-energy, shown in Fig. 18, strong deviations are observed in both cases.

1. Neglecting the asymptotics

Let us now discuss the importance of considering asymptotic functions in numerical implementations. In this regard, we present in Fig. 19 results for $\text{Im}\Sigma(i\nu_0)/U^2$ as a function of U calculated by fRG and PA, with and without asymptotic functions, and compare them with the exact ED data. For these calculations, a frequency grid of $64 \times 64 \times 128$ Matsubara frequencies was used for the reducible vertex functions. In the large frequency domain, we used Eq. (9) and $\Phi_{r,\text{asympt.}} \approx 0$ respectively.

We observe that the results for both, fRG and PA, are strongly affected if we include the asymptotic functions in the calculations: The comparison with the exact result improves by a substantial amount. This is a strong indication of the importance of a correct description of the high-frequency part of the vertex function in all vertex-based numerical implementations.

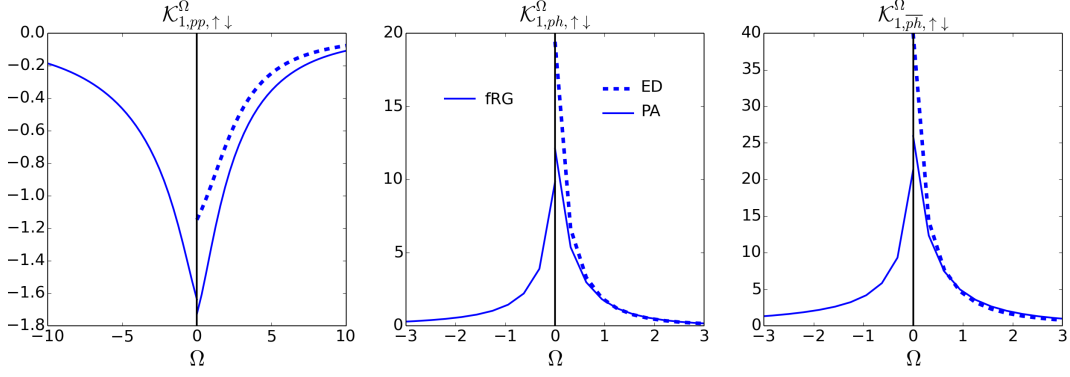
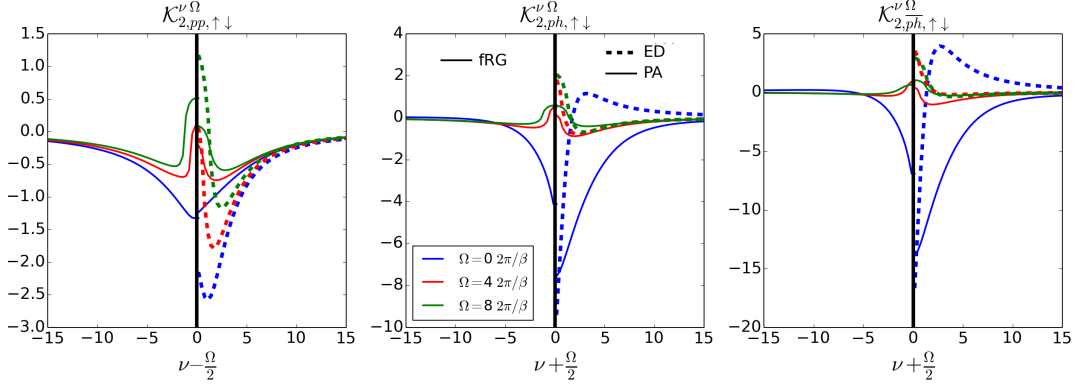
2. Higher order corrections in fRG

In this subsection, we provide a quantitative comparison between the SIAM results as obtained by means of fRG in its one- and two-loop implementation⁴⁴. To this aim, we compare in Fig. 20 the quantities $\mathcal{K}_{1,ph,\uparrow\downarrow}^{\Omega=0}$, $\mathcal{K}_{2,ph,\uparrow\downarrow}^{\nu_0(\Omega=0)}$, as well as $\max_{\nu\nu'} |\mathcal{R}_{ph,\uparrow\downarrow}^{\nu\nu'(\Omega=0)}|$ normalized by their leading order⁹ in U , to the exact ED results as well as to the PA. Consistently to our expectations, we find that the two-loop corrections yield a systematic improvement of the \mathcal{K}_1 , \mathcal{K}_2 and \mathcal{R} functions acquired during the flow, in particular for larger values of the interaction.

More specifically, for $\mathcal{K}_{1,ph,\uparrow\downarrow}$ the two-loop corrections have a minor effect in the weak-coupling regime, whereas an excellent agreement with the exact results is achieved already at the one-loop level. At larger U , the one-loop scheme strongly overestimates $\mathcal{K}_{1,ph,\uparrow\downarrow}$. Here, the two-loop corrections yield a substantial improvement over the one-loop scheme, while underestimating $\mathcal{K}_{1,ph,\uparrow\downarrow}$. We also note the strongly improved agreement of the two-loop fRG with the PA, which is a trend to be expected, since the two-loop scheme allows to include higher orders of the reducible diagrams in an exact way.

As for $\mathcal{K}_{2,ph,\uparrow\downarrow}$, we observe that already in the limit $U \rightarrow 0$ the one-loop scheme *fails* to reproduce the exact result. This can be attributed to the fact that the lowest

⁹ For the particle-hole channel in the $\uparrow\downarrow$ spin configuration the bare bubble vanishes, resulting in a leading order $\mathcal{O}(U^3)$.

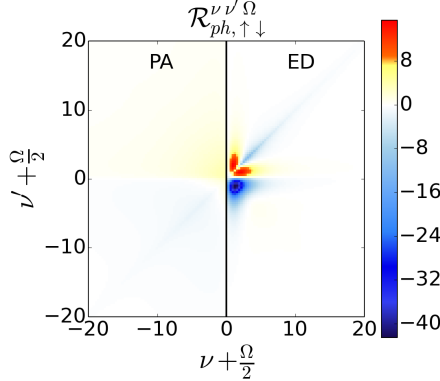
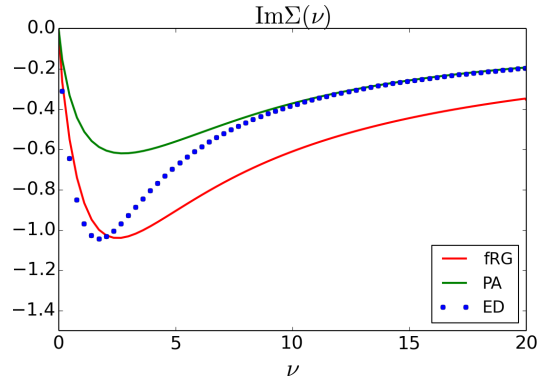
FIG. 15: Same as Fig. 10, but for $U = 4$.FIG. 16: Same as Fig. 11, but for $U = 4$.

order diagram in $\mathcal{K}_{2,ph,\uparrow\downarrow}$ is of order U^3 , and is thus not captured exactly in the one-loop scheme. In particular for the U -flow, we numerically verify the factor $\frac{1}{2}$ (w.r.t. the exact result) already predicted diagrammatically at the end of Sec. IV B, while for the Ω -flow we find, numerically, a factor of ~ 0.89 in all channels. For larger values of U , we observe a behavior similar to the one described for $\mathcal{K}_{1,ph,\uparrow\downarrow}$, that is, a systematic improvement of the results

if the two-loop corrections are included in fRG.

For $\mathcal{R}_{ph,\uparrow\downarrow}$ the trend is similar, while, being a function of $\mathcal{O}(U^4)$, the relative deviations from the exact results increase substantially. The predicted factor $\frac{1}{3}$ for $U \rightarrow 0$ is verified numerically, while for the Ω -flow we find factors 0.78, 0.25 and 0.78 in the pp , ph and $p\bar{h}$ channel respectively.

As for the comparison between the flow-schemes, consistently with the ratios in the weak-coupling regime, we

FIG. 17: Comparison of $\mathcal{R}_{ph,\uparrow\downarrow}$ obtained by means of PA with the exact result. Here, $U = 4$.FIG. 18: Same as Fig. 14, but for $U = 4$.

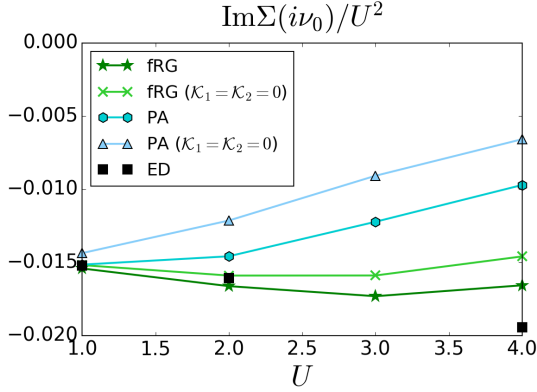


FIG. 19: Comparison of $\text{Im}\Sigma(i\nu_0)/U^2$ for the SIAM with $\beta = 20$ and $\Delta(0) = D = 1$ as obtained by fRG and PA with and without ($\mathcal{K}_1 = \mathcal{K}_2 = 0$) high-frequency asymptotics, compared with ED for $\nu_0 = \frac{\pi}{\beta}$.

observe that the simpler U -flow performs overall worse than the Ω -flow.

3. Efficiency of simplified parametrization schemes

In this subsection we present results for the simplified parametrization scheme⁴¹ presented in Eq. (37). It has found extensive use in the fRG community, as it allows for a substantial speedup of numerical calculations. In the left two panels of Fig. 21 we compare the self-energy at the first Matsubara frequency ($\text{Im}\Sigma(i\nu_0)/U^2$) as well as its tail ($\lim_{\nu \rightarrow \infty} \text{Im}\nu\Sigma(i\nu)/U^2$) for fRG one-loop and two-loop in their full and simplified (\mathcal{K}_{eff}) implementation with PA and the exact results from ED.

For the self-energy at the first Matsubara frequency, we find a good agreement between the simplified parametrization scheme and the fully parametrized fRG implementation for both the one- and two-loop scheme, while the simpler scheme performs slightly worse in reproducing the exact results. In the case of the self-energy tail, the situation is reversed. Here, the aforementioned deviations of the fRG from ED are indeed cured by the simplified parametrization scheme.

To capture the effect of the simplified approximation scheme on the two-particle quantities, we compare in the right panel of Fig. 21 the corresponding susceptibility in the ph -channel for the two-loop case. It is important to note that χ cannot be directly extracted from \mathcal{K}_{eff} using Eq. (10) due to the effective inclusion of \mathcal{K}_2 and \mathcal{R} . Instead, we calculate the susceptibility after the flow by calculating explicitly the bare and vertex-corrected bubble according to equation Eq. (C1b) (VC). This is compared, for an interaction value $U = 4$, to $\chi = \mathcal{K}_1/U^2$ and the corresponding PA and ED data. We find that the simplified parametrization fails to qualitatively reproduce the exact susceptibility, while the other approximations, although underestimating χ , compare qualitatively

well with ED¹⁰.

While the parametrization scheme of Eq. (37) performs well for one-particle quantities, we find that the qualitative features of the susceptibility are badly reproduced. Further, we observe that the ambiguities in the definition of the flow equations for the case of finite temperatures turn out to have a substantial effect on the results for larger values of the interaction. These are strong arguments for the fully parametrized schemes, that capture, consistently, all frequency structures of the two-particle vertex function.

VI. CONCLUSIONS AND OUTLOOK

We have presented a detailed analysis of the diagrammatic content of the two-particle vertex functions, focusing on the terms controlling their high frequency structures. This information is extremely valuable, also at a practical level, because the efficient algorithmic treatment of the vertex asymptotics is fundamental for several recently proposed quantum field theoretical approaches based on expansions around a correlated starting point. In particular, by focusing on the two-particle reducible parts of the vertex function, we could identify the different contributions to their high-frequency asymptotics as diagrammatic classes with a reduced frequency (and momentum) dependence, and establish a connection to the (physical) susceptibilities and the fermion-boson vertices. The gained insights are essential in order to devise efficient parametrization schemes for the two-particle vertex functions. We then discussed the algorithmic details necessary for the implementation of these ideas in numerical (and analytical) studies, considering as specific examples the functional renormalization group approach and the parquet approximation. In order to verify the correct treatment of the high frequency asymptotics, we benchmarked our numerical implementations for a SIAM against exact calculations from ED. Finally, we tested the intrinsic performance of the approaches also in the most challenging strong coupling regime.

This algorithmic progress paves the way towards a full numerical treatment of correlations at the two-particle level, which is pivotal for all vertex-based quantum many-body methods. In particular, these ideas are directly applicable in the treatment of non-local correlations beyond the dynamical mean-field theory by means of its cutting-edge diagrammatic extensions, such as the DF, the DMF2RG, the DFA, and the recently introduced TRILEX and QUADRILEX approach.

¹⁰ We note that χ calculated after the full two-loop flow by means of Eq. (C1) yields a result different from \mathcal{K}_1/U^2 . This is connected to the specific approximations introduced in the fRG, and is absent in the fully self-consistent PA.

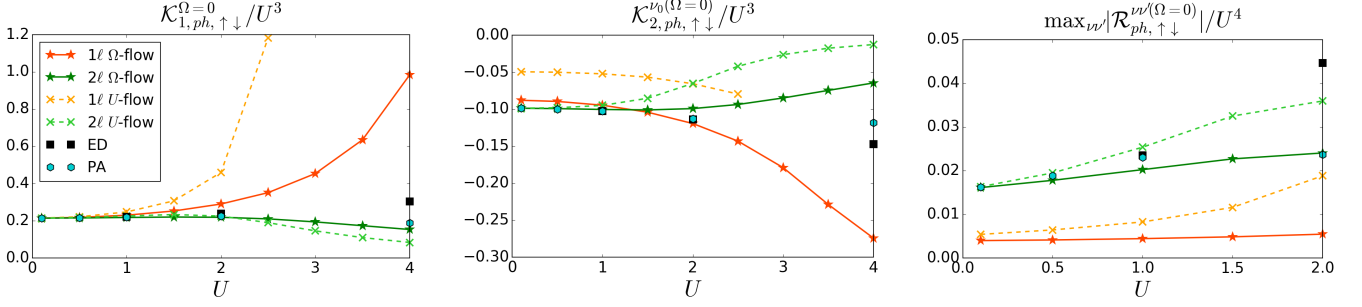


FIG. 20: Comparison of $\mathcal{K}_{1,ph,\uparrow\downarrow}^{\Omega=0}/U^3$, $\mathcal{K}_{2,ph,\uparrow\downarrow}^{\nu_0(\Omega=0)}/U^3$, and $\max_{\nu\nu'} |\mathcal{R}_{ph,\uparrow\downarrow}^{\nu\nu'(\Omega=0)}|/U^4$ ($\nu_0 = \frac{\pi}{\beta}$) for fRG in the one-loop (1ℓ) and two-loop (2ℓ) implementation, for both the Ω - and U -flow, with ED and PA. We note that the one-loop U -flow diverges for $U = 3$ or larger.

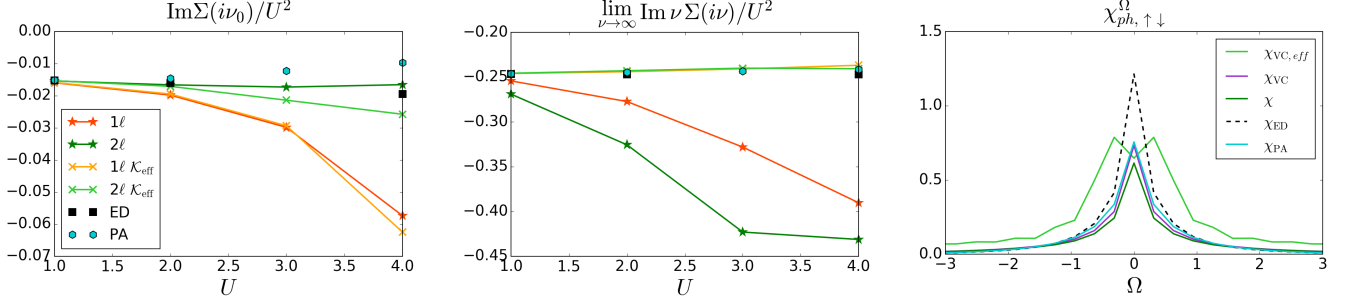


FIG. 21: Left two panels: Comparison of $\text{Im}\Sigma(i\nu_0)/U^2$ and $\lim_{\nu \rightarrow \infty} \text{Im} \nu \Sigma(i\nu)/U^2$ for fRG one-loop and two-loop with the corresponding simplified schemes introduced previously (\mathcal{K}_{eff} , see Eq. (37)), PA and ED. Right panel: Comparison of the susceptibility χ in the ph -channel for $U = 4$ as obtained by means of Eq. (C1b) after the two-loop fRG flow (χ_{VC}) in the conventional and the simplified scheme (eff). This is compared to the susceptibility χ obtained directly from Eq. (10) as well as the PA and ED result.

Acknowledgments

We are grateful to A. Antipov, T. Ayrar, E. Di Napoli, A. Eberlein, C. Honerkamp, A. Katanin, W. Metzner, O. Parcollet, D. Rohe, T. Schäfer, P. Thunström, A. Valli, and D. Vilardi for valuable discussions. We further thank A. Eberlein and T. Ayrar for critical reading of the manuscript. We acknowledge financial support from the Deutsche Forschungsgemeinschaft (DFG) through FOR 723, ZUK 63, and SFB/TRR 21, the Austrian Science Fund (FWF) within the Project F41 (SFB ViCoM), and the European Research Council (ERC) under the European Unions Seventh Framework Program (FP/2007-2013)/ERC through Grant No. 306447 (G.L., K.H.). Calculations were performed on the Vienna Scientific Cluster (VSC).

Appendix A: Notations

In this appendix we present the definitions of the two-particle Green's and (1PI) vertex functions following the notation of Refs. [4,18,48], and further specify the notations used throughout this paper. Let us start by defining

the two-particle Green's function G_2 , which reads

$$G_{2,\sigma_1\sigma_2\sigma_3\sigma_4}(x_1, x_2, x_3, x_4) = \langle \mathcal{T}(c_{\sigma_1}^\dagger(x_1)c_{\sigma_2}(x_2)c_{\sigma_3}^\dagger(x_3)c_{\sigma_4}(x_4)) \rangle. \quad (\text{A1})$$

Here, c^\dagger (c) represent the fermionic creation (annihilation) operators with an associated spin $\sigma = \{\uparrow, \downarrow\}$, the brackets $\langle \dots \rangle$ imply a thermal expectation value, \mathcal{T} denotes the time-ordering operator, and $x = (\mathbf{R}_i, \tau)$ is a four-vector including the lattice site \mathbf{R}_i and the imaginary time τ . First, we note that the number of spin combinations can be reduced by considering spin conservation and the antisymmetry of the two-particle Green's function, allowing us to consider only

$$G_{2,\sigma\sigma'}(x_1, x_2, x_3, x_4) = G_{2,\sigma\sigma'\sigma'\sigma}(x_1, x_2, x_3, x_4). \quad (\text{A2})$$

Further, by making use of time and space-translational invariance, we can always shift all arguments such that $x_4 = 0$. This property can be exploited to yield momen-

tum and frequency conservation, i.e.

$$G_{2,\sigma\sigma'}^{k_1 k_2 k_3 k_4} = \beta V_{\text{BZ}} \delta_{k_1+k_3, k_2+k_4} \times \underbrace{\oint \prod_{i=1}^3 dx_i G_{2,\sigma\sigma'}(x_1, x_2, x_3, 0) e^{-ik_1 x_1} e^{ik_2 x_2} e^{-ik_3 x_3}}_{G_{2,\sigma\sigma'}^{k_1 k_2 k_3}}, \quad (\text{A3})$$

where $k = (\nu, \mathbf{k})$ represents the four-vector with momentum \mathbf{k} and Matsubara frequency ν . Here, we in-

roduced the generalized four-vector integration $\oint dx = \sum_{\mathbf{R}_i} \int_0^\beta d\tau$, that combines the lattice-site summation with the imaginary time integration. The corresponding object in dual space reads $\oint dk = \frac{1}{V_{\text{BZ}}} \int_{\text{BZ}} d\mathbf{k} \frac{1}{\beta} \sum_{i\nu}$, where BZ denotes the first Brillouin zone with a volume V_{BZ} .

To obtain the two-particle vertex function F , we subtract the two possible contractions of the composite operator within the brackets (all disconnected diagrams) and subsequently cut the external fermionic legs. This yields

$$F_{\sigma\sigma'}^{k_1 k_2 k_3 k_4} = -G^{-1}(k_1) G^{-1}(k_3) \underbrace{\left[G_{2,\sigma\sigma'}^{k_1 k_2 k_3 k_4} - G(k_1) G(k_3) (\delta_{k_1, k_2} - \delta_{k_1, k_4} \delta_{\sigma, \sigma'}) \right]}_{G_{2,c,\sigma\sigma'}^{k_1 k_2 k_3 k_4}} G^{-1}(k_2) G^{-1}(k_4). \quad (\text{A4})$$

Here, the additional minus sign is a matter of convention, which is commonly introduced such that the lowest order contribution of F is given by U . Note that $SU(2)$ symmetry is here and in the following explicitly assumed.

While so far we considered the two-particle Green and vertex function with purely fermionic arguments, one often introduces ‘mixed’ notations using a bosonic and two fermionic arguments, in order to highlight a specific scattering channel. The adoption of these notations is essential for the decomposition scheme presented in this paper, in particular for the reducible vertex functions. Hence, we introduce the particle-particle (pp) notation

$$F_{pp,\sigma\sigma'}^{kk'q} = F_{\sigma\sigma'}^{k(q-k')(q-k)k'} \quad (\text{A5})$$

the particle-hole (ph) notation

$$F_{ph,\sigma\sigma'}^{kk'q} = F_{\sigma\sigma'}^{k(k+q)(k'+q)k'} \quad (\text{A6})$$

and the transverse particle-hole (\overline{ph}) notation

$$F_{\overline{ph},\sigma\sigma'}^{kk'q} = F_{\sigma\sigma'}^{k k' (k'+q)(k+q)}, \quad (\text{A7})$$

which are defined correspondingly for G_2 and the other vertex functions ϕ , $\Lambda_{2\text{PI}}$ and Γ (see Sec.II). A diagrammatic representation of the three notations is shown in Fig. 22. Let us note that in general, for the two-particle vertex F and also for the fully irreducible vertex $\Lambda_{2\text{PI}}$, none of these notations is a priori more favorable, each of them just being an alternative way to look at the same physical object⁴⁸.

Finally, we introduce susceptibilities in all scattering

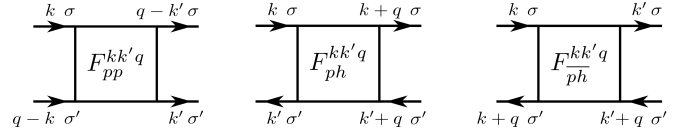


FIG. 22: Notations of the vertex functions in the three different scattering channels.

channels,

$$\chi_{pp,\sigma\sigma'}^{kk'q} = \oint dk dk' G_{2,c,pp,\sigma\sigma'}^{kk'q} + \oint dk G(q-k) G(k), \quad (\text{A8a})$$

$$\chi_{ph,\sigma\sigma'}^{kk'q} = \oint dk dk' G_{2,c,ph,\sigma\sigma'}^{kk'q} - \delta_{\sigma,\sigma'} \oint dk G(k) G(k+q), \quad (\text{A8b})$$

$$\chi_{\overline{ph},\sigma\sigma'}^{kk'q} = \oint dk dk' G_{2,c,\overline{ph},\sigma\sigma'}^{kk'q} + \oint dk G(k) G(k+q). \quad (\text{A8c})$$

They can be easily combined to yield the physical susceptibilities in the density, magnetic, singlet and triplet channel⁴.

Appendix B: Explicit equations

We here want to present some explicit forms of the parquet equations presented schematically in Sec. IV C. Let us begin by showing the Bethe Salpeter equations in

their spin-resolved version.¹¹

¹¹ We want to point out the fond similarity between Eqs. (B1), which are the basis for the iterative parquet approximation solver, and the channel-resolved fRG flow Eqs. (33), which technically allows for very similar implementations of the two approaches.

$$\Phi_{pp,\uparrow\downarrow}^{kk'q} = \oint dk'' G(k'')G(q-k'') \times \Gamma_{pp,\uparrow\downarrow}^{kk''q} F_{pp,\uparrow\downarrow}^{k''k'q}, \quad (\text{B1a})$$

$$\Phi_{ph,\uparrow\downarrow}^{kk'q} = - \oint dk'' G(k''+q)G(k'') \times \left[\Gamma_{ph,\uparrow\downarrow}^{kk''q} F_{ph,\uparrow\downarrow}^{k''k'q} + \Gamma_{ph,\uparrow\downarrow}^{kk''q} F_{ph,\uparrow\downarrow}^{k''k'q} \right], \quad (\text{B1b})$$

$$\Phi_{\overline{ph},\uparrow\downarrow}^{kk'q} = \oint dk'' G(k''+q)G(k'') \times \Gamma_{\overline{ph},\uparrow\downarrow}^{kk''q} F_{\overline{ph},\uparrow\downarrow}^{k''k'q}. \quad (\text{B1c})$$

In the $SU(2)$ symmetric case they can be diagonalized by introducing the density (d), magnetic (m), singlet (s) and triplet (t) channel as introduced in Sec. IV C,

$$\Phi_{d/m}^{kk'q} = \oint dk'' G(k''+q)G(k'') \times \Gamma_{d/m}^{kk''q} F_{d/m}^{k''k'q}, \quad (\text{B2a})$$

$$\Psi_{t/s}^{kk'q} = \pm \frac{1}{2} \oint dk'' G(k'')G(q-k'') \times \Gamma_{s/t}^{kk''q} F_{s/t}^{k''k'q}. \quad (\text{B2b})$$

Given the fully irreducible vertex function $\Lambda^{kk'q}$, the other two-particle vertex function can be calculated through the parquet equations as shown below:

$$F_d^{kk'q} = \Lambda_d^{kk'q} + \Phi_d^{kk'q} - \frac{1}{2}\Phi_d^{k(k+q)(k'-k)} - \frac{3}{2}\Phi_m^{k(k+q)(k'-k)} + \frac{1}{2}\Psi_s^{kk'(k+k'+q)} + \frac{3}{2}\Psi_t^{kk'(k+k'+q)}, \quad (\text{B3a})$$

$$F_m^{kk'q} = \Lambda_m^{kk'q} + \Phi_m^{kk'q} - \frac{1}{2}\Phi_d^{k(k+q)(k'-k)} + \frac{1}{2}\Phi_m^{k(k+q)(k'-k)} - \frac{1}{2}\Psi_s^{kk'(k+k'+q)} + \frac{1}{2}\Psi_t^{kk'(k+k'+q)}, \quad (\text{B3b})$$

$$F_s^{kk'q} = \Lambda_s^{kk'q} + \Psi_s^{kk'q} + \frac{1}{2}\Phi_d^{k(q-k')(k'-k)} - \frac{3}{2}\Phi_m^{k(q-k')(k'-k)} + \frac{1}{2}\Phi_d^{kk'(q-k-k')} - \frac{3}{2}\Phi_m^{kk'(q-k-k')}, \quad (\text{B3c})$$

$$F_t^{kk'q} = \Lambda_t^{kk'q} + \Psi_t^{kk'q} - \frac{1}{2}\Phi_d^{k(q-k')(k'-k)} - \frac{1}{2}\Phi_m^{k(q-k')(k'-k)} + \frac{1}{2}\Phi_d^{kk'(q-k-k')} + \frac{1}{2}\Phi_m^{kk'(q-k-k')}. \quad (\text{B3d})$$

Similarly, the channel-dependent irreducible two-particle vertex $\Gamma_r^{kk'q}$ is obtained as $\Gamma_r^{kk'q} = F_r^{kk'q} - \Phi_r^{kk'q}$.

Appendix C: Extracting asymptotics from F

In this part we describe an approach that extracts the asymptotic functions directly from the full vertex function F . This procedure was employed to acquire all pre-

sented high-frequency results for the ED vertices, and is based on the fact that one can write down explicit Feynman diagrams for all asymptotic functions. These consist of all possible ways of pinching two external legs of F into one bare vertex $U^{6,30}$. Since the latter is purely local in space and time, the dependence on two fermionic arguments is replaced by a single bosonic (transfer) one. The resulting diagrams for \mathcal{K}_1 are shown in Fig. 23, and read explicitly

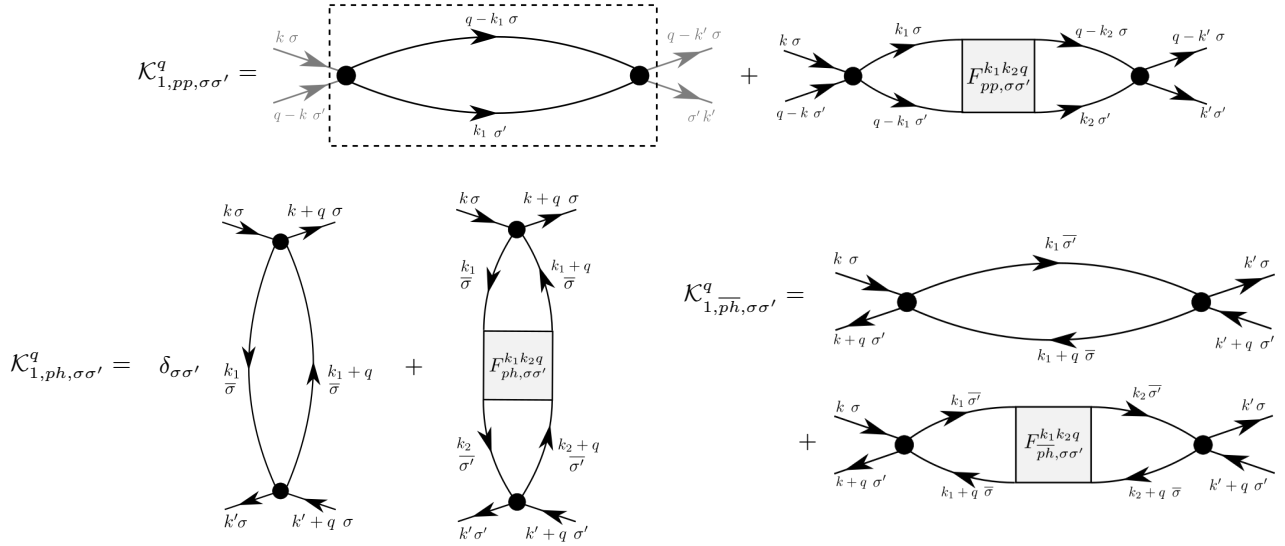


FIG. 23: Diagrammatic representation of the \mathcal{K}_1 functions in the three different channels. As denoted in the first diagram, the external lines are to be excluded, making the k and k' arguments redundant. Here, $\bar{\sigma}$ denotes the opposite spin of σ , and $SU(2)$ symmetry is explicitly assumed.

$$\mathcal{K}_{1,pp,\sigma\sigma'}^q = U^2 \oint dk_i G(k_1) G(q - k_1) F_{pp,\sigma\sigma'}^{k_1 k_2 q} G(q - k_2) G(k_2) - U^2 \oint dk_1 G(q - k_1) G(k_1), \quad (C1a)$$

$$\mathcal{K}_{1,ph,\sigma\sigma'}^q = U^2 \oint dk_i G(k_1) G(k_1 + q) F_{ph,\sigma\sigma'}^{k_1 k_2 q} G(k_2) G(k_2 + q) + U^2 \delta_{\sigma,\sigma'} \oint dk_1 G(k_1) G(k_1 + q), \quad (C1b)$$

$$\mathcal{K}_{1,\overline{ph},\sigma\sigma'}^q = U^2 \oint dk_i G(k_1) G(k_1 + q) F_{\overline{ph},\sigma\sigma'}^{k_1 k_2 q} G(k_2) G(k_2 + q) - U^2 \oint dk_1 G(k_1) G(k_1 + q). \quad (C1c)$$

Here $\bar{\sigma}$ denotes the opposite spin of σ , and $SU(2)$ symmetry is explicitly assumed. In the case of \mathcal{K}_2 one introduces just one additional bare vertex, as shown in Fig. 24. Note that here, the previously determined \mathcal{K}_1 has to be subtracted. The equations in all scattering channels then read

$$\mathcal{K}_{2,pp,\sigma\sigma'}^{kq} = -U \oint dk_1 G(q - k_1) F_{pp,\sigma\sigma'}^{k k_1 q} G(k_1) - \mathcal{K}_{1,pp,\sigma\sigma'}^q, \quad (C2a)$$

$$\mathcal{K}_{2,ph,\sigma\sigma'}^{kq} = U \oint dk_1 G(k_1) F_{ph,\sigma\sigma'}^{k k_1 q} G(k_1 + q) - \mathcal{K}_{1,ph,\sigma\sigma'}^q, \quad (C2b)$$

$$\mathcal{K}_{2,\overline{ph},\sigma\sigma'}^{kq} = -U \oint dk_1 G(k_1) G(k_1 + q) \times \left[\delta_{\sigma\sigma'} F_{\overline{ph},\uparrow\downarrow}^{k k_1 q} + (1 - \delta_{\sigma\sigma'}) F_{\overline{ph},\uparrow\uparrow}^{k k_1 q} \right] - \mathcal{K}_{1,\overline{ph},\sigma\sigma'}^q. \quad (C2c)$$

Further, by exploiting the symmetry relations shown in Appendix D, one can easily derive $\bar{\mathcal{K}}_2$ from \mathcal{K}_2 . [b]

As it is typical within an ED algorithm for a SIAM, the values for F are known numerically for a finite grid in the frequency domain. Thus, in the first calculation of the aforementioned diagrams according to Eqs. (C1) and (C2) we have to make a rough approximation for F (i.e. $F = U$) in the large-frequency domain, which will introduce an error. To improve on this ‘one-shot’ calculation of the diagrams, we exploit a self-consistent scheme:

- I: Initialize the \mathcal{K}_1 ’s and \mathcal{K}_2 ’s to 0. Their grids may

deviate from the grid for F .

- II: Calculate a set of new \mathcal{K}_1 ’s and \mathcal{K}_2 ’s according to Eqs. (C1) and (C2).
- III: Rebuild the vertex in an arbitrarily large region (as needed) using the updated asymptotic functions.
- IV: Continue from II till convergence

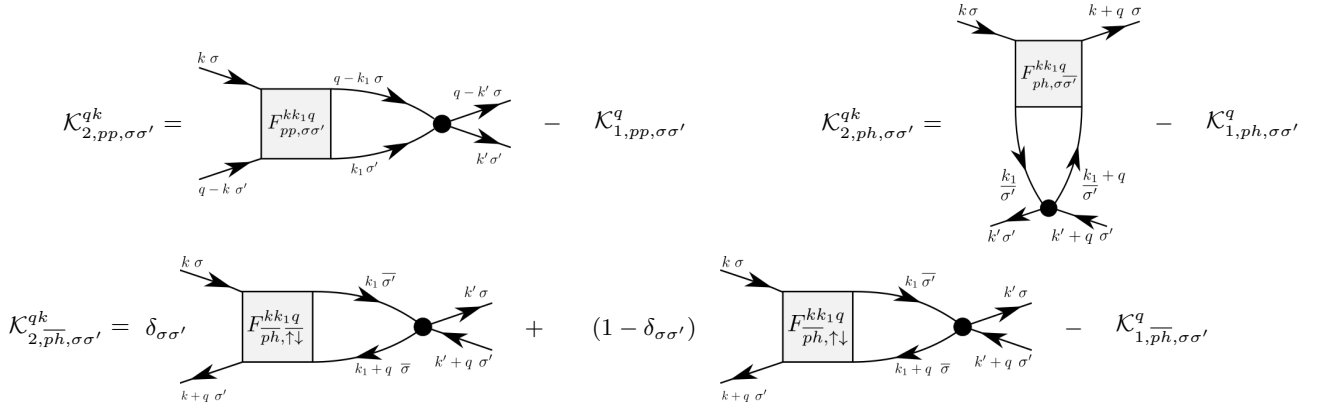


FIG. 24: Diagrammatic representation of the \mathcal{K}_2 functions in the three different channels. Here, $\bar{\sigma}$ denotes the opposite spin of σ , while $SU(2)$ symmetry is explicitly assumed.

Once the asymptotic functions are fully converged, we can directly determine the localized structures using

$$\Lambda_{2\text{PI}} + \sum_r \mathcal{R}_r = F - \left(\sum_r \mathcal{K}_{1,r} + \mathcal{K}_{2,r} + \bar{\mathcal{K}}_{2,r} \right). \quad (\text{C3})$$

Further, since, at this point, we have F available in the full frequency domain, we can use this additional information to determine also all the Φ functions on an arbitrarily large frequency grid by means of the Bethe-Salpeter equations (4). If needed, \mathcal{R} and $\Lambda_{2\text{PI}}$ can then be determined by Eq. (13) and Eq. (2) respectively.

The approach described in this section was used to compute all the exact asymptotic functions and reducible vertices presented in Sec. V, from ED calculations, originally performed on a fermionic frequency grid of $128 \times 128 \times 128$ Matsubara frequencies. While here we are dealing with a purely local vertex, we stress that this approach is equally applicable in the non-local case.

Appendix D: Symmetries

1. Symmetries of \mathcal{K}_1 and \mathcal{K}_2

In this section we summarize the symmetries of the previously introduced asymptotic functions. Before addressing the specific physical symmetries of the system of our interest, which provide useful relations for \mathcal{K}_1 and \mathcal{K}_2 , we provide some fundamental relations which hold^{1,4,6} independently of the system under analysis. First, we consider the exchange of two (fermionic) annihilation operators in the time-ordered matrix element of Eq. (A3), which, as a consequence of the Pauli-principle, yields a minus sign (also referred to as ‘crossing symmetry’^{1,4,6}). Diagrammatically speaking, this corresponds to an exchange of two outgoing lines. For \mathcal{K}_1 , this operation leads

to the following relations:

$$\mathcal{K}_{1,pp,\sigma\sigma'}^q = -\mathcal{K}_{1,pp,\bar{\sigma}\bar{\sigma}'}^q \quad (\text{D1a})$$

$$\mathcal{K}_{1,ph,\sigma\sigma'}^q = -\mathcal{K}_{1,\bar{p}h,\bar{\sigma}\bar{\sigma}'}^q \quad (\text{D1b})$$

$$\mathcal{K}_{1,\bar{p}h,\sigma\sigma'}^q = -\mathcal{K}_{1,ph,\bar{\sigma}\bar{\sigma}'}^q. \quad (\text{D1c})$$

Here, $\bar{\sigma}\bar{\sigma}'$ denotes a spin configuration of the external indices where spins are crossing. While for the pp channel one finds relations between different spin configurations within the same channel, the ph and $\bar{p}h$ -channel are interchanged. Similarly, for \mathcal{K}_2 one finds:

$$\mathcal{K}_{2,pp,\sigma\sigma'}^{kq} = -\mathcal{K}_{2,pp,\bar{\sigma}\bar{\sigma}'}^{kq} \quad (\text{D2a})$$

$$\mathcal{K}_{2,ph,\sigma\sigma'}^{kq} = -\mathcal{K}_{2,\bar{p}h,\bar{\sigma}\bar{\sigma}'}^{kq} \quad (\text{D2b})$$

$$\mathcal{K}_{2,\bar{p}h,\sigma\sigma'}^{kq} = -\mathcal{K}_{2,ph,\bar{\sigma}\bar{\sigma}'}^{kq}. \quad (\text{D2c})$$

A second generic operation involves the simultaneous exchange of both annihilation and creation operators in Eq. A3. Diagrammatically, this corresponds to an exchange of both the incoming and outgoing particles. In this case we end up with the following relations for \mathcal{K}_1 :

$$\mathcal{K}_{1,pp,\sigma\sigma'}^q = \mathcal{K}_{1,pp,\sigma'\sigma}^q \quad (\text{D3a})$$

$$\mathcal{K}_{1,ph,\sigma\sigma'}^q = \mathcal{K}_{1,ph,\sigma'\sigma}^{-q} \quad (\text{D3b})$$

$$\mathcal{K}_{1,\bar{p}h,\sigma\sigma'}^q = \mathcal{K}_{1,\bar{p}h,\sigma'\sigma}^{-q}. \quad (\text{D3c})$$

For \mathcal{K}_2 one obtains:

$$\mathcal{K}_{2,pp,\sigma\sigma'}^{kq} = \mathcal{K}_{2,pp,\sigma'\sigma}^{(q-k)q} \quad (\text{D4a})$$

$$\mathcal{K}_{2,ph,\sigma\sigma'}^{kq} = \mathcal{K}_{2,ph,\sigma'\sigma}^{(k+q)(-q)} \quad (\text{D4b})$$

$$\mathcal{K}_{2,\bar{p}h,\sigma\sigma'}^{kq} = \mathcal{K}_{2,\bar{p}h,\sigma'\sigma}^{(k+q)(-q)}. \quad (\text{D4c})$$

While for this operation all the corresponding channels are conserved, the diagrammatic class changes from \mathcal{K}_2 to $\bar{\mathcal{K}}_2$ in the case of the ph and $\bar{p}h$ channel.

Symmetries	$\mathcal{K}_{1,r}$	$\mathcal{K}_{2,r}$
SU(2)	$\mathcal{K}_{1,r,\sigma\sigma'}^q = \mathcal{K}_{1,r,\bar{\sigma}\bar{\sigma}'}^q$ $\mathcal{K}_{1,r,\sigma\sigma}^q = \mathcal{K}_{1,r,\sigma\sigma'}^q + \mathcal{K}_{1,r,\bar{\sigma}\bar{\sigma}'}^q$	$\mathcal{K}_{2,r,\sigma\sigma'}^{kq} = \mathcal{K}_{2,r,\bar{\sigma}\bar{\sigma}'}^{kq}$ $\mathcal{K}_{2,r,\sigma\sigma}^{kq} = \mathcal{K}_{2,r,\sigma\sigma'}^{kq} + \mathcal{K}_{2,r,\bar{\sigma}\bar{\sigma}'}^{kq}$
Time reversal	$\mathcal{K}_{1,r,\sigma\sigma'}^q = \mathcal{K}_{1,r,\sigma'\sigma}^q$	$\mathcal{K}_{2,r,\sigma\sigma'}^{kq} = \bar{\mathcal{K}}_{2,r,\sigma\sigma'}^{kq}$
Particle hole	$\left(\mathcal{K}_{1,r,\sigma\sigma'}^q\right)^* = \mathcal{K}_{1,r,\sigma\sigma'}^{(\Omega,-\mathbf{q})}$	$\left(\mathcal{K}_{2,r,\sigma\sigma'}^{kq}\right)^* = \mathcal{K}_{2,r,\sigma\sigma'}^{(\nu,\mathbf{\Pi}-\mathbf{k})(\Omega,-\mathbf{q})}$

TABLE I: Symmetry table for \mathcal{K}_1 and \mathcal{K}_2 . Here, $\mathbf{\Pi} = (\pi, \pi, \dots)$ represents the (d -dimensional) 'antiferromagnetic momentum' in the case of a simple (hyper)cubic lattice with lattice constant $a = 1$.

To conclude the discussion of the fundamental relations, we consider the complex conjugation operation, that leads to the following relations for \mathcal{K}_1 :

$$\left(\mathcal{K}_{1,pp,\sigma\sigma'}^q\right)^* = \mathcal{K}_{1,pp,\sigma'\sigma}^{-q} \quad (\text{D5a})$$

$$\left(\mathcal{K}_{1,ph,\sigma\sigma'}^q\right)^* = \mathcal{K}_{1,ph,\sigma'\sigma}^{-q} \quad (\text{D5b})$$

$$\left(\mathcal{K}_{1,\bar{p}\bar{h},\sigma\sigma'}^q\right)^* = \mathcal{K}_{1,\bar{p}\bar{h},\sigma'\sigma}^q, \quad (\text{D5c})$$

and for \mathcal{K}_2 :

$$\left(\mathcal{K}_{2,pp,\sigma\sigma'}^{kq}\right)^* = \mathcal{K}_{2,pp,\sigma'\sigma}^{(-k)(-q)} \quad (\text{D6a})$$

$$\left(\mathcal{K}_{2,ph,\sigma\sigma'}^{kq}\right)^* = \mathcal{K}_{2,ph,\sigma'\sigma}^{(-k)(-q)} \quad (\text{D6b})$$

$$\left(\mathcal{K}_{2,\bar{p}\bar{h},\sigma\sigma'}^{kq}\right)^* = \mathcal{K}_{2,\bar{p}\bar{h},\sigma'\sigma}^{(-k-q)q}. \quad (\text{D6c})$$

Using these fundamental relations, we can formulate the system-related physical symmetries, namely $SU(2)$, time reversal and particle-hole symmetry, in a channel-independent way. The results are summarized in Table I. Note that for the particle-hole symmetry, the relations differ for the frequency and momentum dependence. While in the purely local case, this symmetry implies a vanishing imaginary part of all two-particle quantities, this holds only for specific lattice-dependent \mathbf{k} vectors in the non-local case.

2. Symmetries of \mathcal{R}

For the sake of completeness we report the symmetries of the remaining diagrammatic class, namely the rest function \mathcal{R} , which hold equally for the reducible vertex functions Φ . As shown above, the first set of fundamental relations results from exchanging two outgoing particles. We find the following relations for \mathcal{R} in the

different channels:

$$\mathcal{R}_{pp,\sigma\sigma'}^{kk'q} = -\mathcal{R}_{pp,\sigma\sigma'}^{(k)(q-k')q} \quad (\text{D7a})$$

$$\mathcal{R}_{ph,\sigma\sigma'}^{kk'q} = -\mathcal{R}_{ph,\sigma\sigma'}^{k'q} \quad (\text{D7b})$$

$$\mathcal{R}_{\bar{p}\bar{h},\sigma\sigma'}^{kk'q} = -\mathcal{R}_{\bar{p}\bar{h},\sigma\sigma'}^{kk'q}. \quad (\text{D7c})$$

By means of the simultaneous exchange of both incoming and outgoing particles we obtain:

$$\mathcal{R}_{pp,\sigma\sigma'}^{kk'q} = \mathcal{R}_{pp,\sigma'\sigma}^{(q-k)(q-k')q} \quad (\text{D8a})$$

$$\mathcal{R}_{ph,\sigma\sigma'}^{kk'q} = \mathcal{R}_{ph,\sigma'\sigma}^{(k'+q)(k+q)(-q)} \quad (\text{D8b})$$

$$\mathcal{R}_{\bar{p}\bar{h},\sigma\sigma'}^{kk'q} = \mathcal{R}_{\bar{p}\bar{h},\sigma'\sigma}^{(k'+q)(k+q)(-q)}. \quad (\text{D8c})$$

Finally, the complex conjugation operation leads to the following relations:

$$\left(\mathcal{R}_{pp,\sigma\sigma'}^{kk'q}\right)^* = \mathcal{R}_{pp,\sigma\sigma'}^{(-k')(-k)(-q)} \quad (\text{D9a})$$

$$\left(\mathcal{R}_{ph,\sigma\sigma'}^{kk'q}\right)^* = \mathcal{R}_{ph,\sigma\sigma'}^{(-k')(-k)(-q)} \quad (\text{D9b})$$

$$\left(\mathcal{R}_{\bar{p}\bar{h},\sigma\sigma'}^{kk'q}\right)^* = \mathcal{R}_{\bar{p}\bar{h},\sigma\sigma'}^{(-k-q)(-k'-q)q}. \quad (\text{D9c})$$

Symmetries	\mathcal{R}_r
SU(2)	$\mathcal{R}_{r,\sigma\sigma'}^{kk'q} = \mathcal{R}_{r,\bar{\sigma}\bar{\sigma}'}^{kk'q}$ $\mathcal{R}_{r,\sigma\sigma}^{kk'q} = \mathcal{R}_{r,\sigma\sigma'}^{kk'q} + \mathcal{R}_{r,\bar{\sigma}\bar{\sigma}'}^{kk'q}$
Time reversal	$\mathcal{R}_{r,\sigma\sigma'}^{kk'q} = \mathcal{R}_{r,\sigma'\sigma}^{k'kq}$
Particle hole	$\left(\mathcal{R}_{r,\sigma\sigma'}^{kk'q}\right)^* = \mathcal{R}_{r,\sigma\sigma'}^{(\nu,\mathbf{\Pi}-\mathbf{k})(\nu',\mathbf{\Pi}-\mathbf{k}')(\Omega,-\mathbf{q})}$

In the same way as for \mathcal{K}_1 and \mathcal{K}_2 , the fundamental relations for \mathcal{R} allow us to express the physical symmetries in a channel-independent way, see Table II.

- ¹ N. Bickers, in *Theoretical Methods for Strongly Correlated Electrons*, edited by D. Sènèchal, A.-M. Tremblay, and C. Bourbonnais (Springer New York, 2004), CRM Series in Mathematical Physics, pp. 237–296, ISBN 978-0-387-00895-0.
- ² A. N. Tahvildar-Zadeh, J. K. Freericks, and M. Jarrell, Phys. Rev. B **55**, 942 (1997).
- ³ J. Kuneš, Phys. Rev. B **83**, 085102 (2011).
- ⁴ G. Rohringer, A. Valli, and A. Toschi, Phys. Rev. B **86**, 125114 (2012).
- ⁵ M. Kinza, J. Ortloff, J. Bauer, and C. Honerkamp, Phys. Rev. B **87**, 035111 (2013).
- ⁶ G. Rohringer, Ph.D. thesis, Vienna University of Technology (2014).
- ⁷ S. Hummel, Master's thesis, Vienna University of Technology (2014).
- ⁸ G. Li, N. Wentzell, P. Pudleiner, P. Thunström, and K. Held, Phys. Rev. B **93**, 165103 (2016).
- ⁹ W. Metzner, M. Salmhofer, C. Honerkamp, V. Meden, and K. Schönhammer, Rev. Mod. Phys. **84**, 299 (2012).
- ¹⁰ C. D. Dominicis and P. C. Martin, J. Math. Phys. **5**, 14 (1964).
- ¹¹ C. D. Dominicis and P. C. Martin, J. Math. Phys. **5**, 31 (1964).
- ¹² V. Janiš, Phys. Rev. B **60**, 11345 (1999).
- ¹³ A. Toschi, A. A. Katanin, and K. Held, Phys. Rev. B **75**, 045118 (2007).
- ¹⁴ A. A. Katanin, A. Toschi, and K. Held, Phys. Rev. B **80**, 075104 (2009).
- ¹⁵ G. Rohringer, A. Toschi, A. Katanin, and K. Held, Phys. Rev. Lett. **107**, 256402 (2011).
- ¹⁶ T. Schäfer, F. Geles, D. Rost, G. Rohringer, E. Arrigoni, K. Held, N. Blümer, M. Aichhorn, and A. Toschi, Phys. Rev. B **91**, 125109 (2015).
- ¹⁷ A. Valli, T. Schäfer, P. Thunström, G. Rohringer, S. Andergassen, G. Sangiovanni, K. Held, and A. Toschi, Phys. Rev. B **91**, 115115 (2015).
- ¹⁸ G. Rohringer, A. Toschi, H. Hafermann, K. Held, V. I. Anisimov, and A. A. Katanin, Phys. Rev. B **88**, 115112 (2013).
- ¹⁹ C. Taranto, S. Andergassen, J. Bauer, K. Held, A. Katanin, W. Metzner, G. Rohringer, and A. Toschi, Phys. Rev. Lett. **112**, 196402 (2014).
- ²⁰ A. E. Antipov, E. Gull, and S. Kirchner, Phys. Rev. Lett. **112**, 226401 (2014).
- ²¹ A. N. Rubtsov, M. I. Katsnelson, and A. I. Lichtenstein, Phys. Rev. B **77**, 033101 (2008).
- ²² A. N. Rubtsov, M. I. Katsnelson, A. I. Lichtenstein, and A. Georges, Phys. Rev. B **79**, 045133 (2009).
- ²³ H. Hafermann, G. Li, A. N. Rubtsov, M. I. Katsnelson, A. I. Lichtenstein, and H. Monien, Phys. Rev. Lett. **102**, 206401 (2009).
- ²⁴ N. Wentzell, C. Taranto, A. Katanin, A. Toschi, and S. Andergassen, Phys. Rev. B **91**, 045120 (2015).
- ²⁵ G. Li, Phys. Rev. B **91**, 165134 (2015).
- ²⁶ T. Ayral and O. Parcollet, Phys. Rev. B **92**, 115109 (2015).
- ²⁷ T. Ayral and O. Parcollet, Phys. Rev. B **93**, 235124 (2016), 1512.06719.
- ²⁸ T. Ayral and O. Parcollet, Phys. Rev. B **94**, 075159 (2016).
- ²⁹ A. A. Abrikosov, *Methods of Quantum Field Theory in Statistical Physics (Dover Books on Physics)* (Dover Publications, 1975), rev. english ed., ISBN 9780486632285.
- ³⁰ G. Rohringer and A. Toschi, Phys. Rev. B **94**, 125144 (2016).
- ³¹ H. Hafermann, S. Brener, A. N. Rubtsov, M. I. Katsnelson, and A. I. Lichtenstein, JETP Lett. **86**, 677 (2008).
- ³² T. Schäfer, G. Rohringer, O. Gunnarsson, S. Ciuchi, G. Sangiovanni, and A. Toschi, Phys. Rev. Lett. **110**, 246405 (2013).
- ³³ E. Kozik, M. Ferrero, and A. Georges, Phys. Rev. Lett. **114**, 156402 (2015).
- ³⁴ T. Schäfer, S. Ciuchi, M. Wallerberger, P. Thunström, O. Gunnarsson, G. Sangiovanni, G. Rohringer, and A. Toschi, arXiv:1606.03393 (2016).
- ³⁵ T. Ribic, G. Rohringer, and K. Held, Phys. Rev. B **93**, 195105 (2016).
- ³⁶ M. Salmhofer, *Renormalization: An Introduction (Theoretical and Mathematical Physics)* (Springer, Berlin and Heidelberg, 1999), corrected ed., ISBN 9783540646662.
- ³⁷ C. Wetterich, Phys. Lett. B **301**, 90 (1993).
- ³⁸ M. Salmhofer and C. Honerkamp, Prog. Theor. Phys. **105**, 1 (2001).
- ³⁹ K.-U. Giering and M. Salmhofer, Phys. Rev. B **86**, 245122 (2012).
- ⁴⁰ C. Honerkamp, D. Rohe, S. Andergassen, and T. Enss, Phys. Rev. B **70**, 235115 (2004).
- ⁴¹ C. Karrasch, A. Oguri, and V. Meden, Phys. Rev. B **77**, 024517 (2008).
- ⁴² C. Husemann and M. Salmhofer, Phys. Rev. B **79**, 195125 (2009).
- ⁴³ A. A. Katanin, Phys. Rev. B **70**, 115109 (2004).
- ⁴⁴ A. Eberlein, Phys. Rev. B **90**, 115125 (2014).
- ⁴⁵ A. A. Katanin, Phys. Rev. B **79**, 235119 (2009).
- ⁴⁶ S.-X. Yang, H. Fotso, H. Hafermann, K.-M. Tam, J. Moreno, T. Pruschke, and M. Jarrell, Phys. Rev. B **84**, 155106 (2011).
- ⁴⁷ V. Janiš and V. Pokorný, Phys. Rev. B **90**, 045143 (2014).
- ⁴⁸ O. Gunnarsson, T. Schäfer, J. P. F. LeBlanc, E. Gull, J. Merino, G. Sangiovanni, G. Rohringer, and A. Toschi, Phys. Rev. Lett. **114**, 236402 (2015).